CORA Cork Open Research Archive
Cartlann Taighde Oscailte Chorcaí

Title	Overcoming Pd–TiO2 deactivation during H2 production from photoreforming using Cu@Pd nanoparticles supported on TiO2
Authors	Platero, F.;López-Martín, A.;Caballero, A.;Rojas, T. C.;Nolan, Michael;Colón, G.
Publication date	2021-03-01
Original Citation	Platero, F., López-Martín, A., Caballero, A., Rojas, T. C., Nolan, M. and Colón, G. (2021) 'Overcoming Pd–TiO2 deactivation during H2 production from photoreforming using Cu@Pd nanoparticles supported on TiO2', ACS Applied Nano Materials, 4(3), pp. 3204-3219. doi: 10.1021/acsanm.1c00345
Type of publication	Article (peer-reviewed)
Link to publisher's version	10.1021/acsanm.1c00345
Rights	© 2021, American Chemical Society. This document is the Accepted Manuscript version of a Published Work that appeared in final form in ACS Applied Nano Materials, after technical editing by the publisher. To access the final edited and published work see: https://doi.org/10.1021/acsanm.1c00345
Download date	2026-11-07 23:21:22
Item downloaded from	https://hdl.handle.net/10468/11230



University College Cork, Ireland
Coláiste na hOllscoile Corcaigh

Overcoming Pd/TiO_2 Deactivation during H_2 Production from Photoreforming by Using Cu@Pd Nanoparticles Supported on TiO_2

*F. Platero[a], A. López-Martín[a], A. Caballero[a], T.C. Rojas[a], M. Nolan[b], G. Colón[a] **

[a] Instituto de Ciencia de Materiales de Sevilla. Centro Mixto Universidad de Sevilla-CSIC. Américo Vespucio s/n. 41092 Sevilla. Spain

[b] Tyndall National Institute, University College Cork, Lee Maltings, Dyke Parade, Cork, T12 R5CP Ireland

ABSTRACT

Different Cu@Pd/TiO_2 systems have been prepared by a two-step synthesis to obtain a bimetallic co-catalyst for H_2 photoreforming reaction. We find that the tailored deposition of Pd covering the Cu nanoclusters by a galvanic replacement process results in the formation of a core@shell structure. The photocatalytic H_2 production after 18 h is 350 mmol/g on Cu@$Pd_{1.0}$/TiO_2 bimetallic system, being higher than on the monometallic ones, with H_2 production of 250 mmol/g for Pd supported TiO_2. Surface characterization from HAADF-STEM, H_2-TPR, CO-FTIR and XPS gives clear evidence of the formation of a core@shell structure. With a Pd loading of 0.2-0.3 at% we propose full coverage of the Cu nanoparticles with Pd. Long time photoreforming runs show the enhanced performance of supported Cu@Pd with respect to bare palladium leading to a more stable catalyst and ultimately higher H_2 production.

KEYWORDS**:** Copper; Palladium; Core-Shell; TiO_2; H_2 Photoreforming; DFT.

* Corresponding author: gcolon@icmse.csic.es

INTRODUCTION

In recent years, H_2 production by the alcohol photoreforming reaction has gained significant interest as a new topic in the field of photocatalysis.[1,2] and is an alternative to water splitting for hydrogen production. Taking into consideration the current socioeconomical and environmental situation, it is now accepted that hydrogen must play the key role in the future energy system since it is considered the ultimate clean energy carrier. Despite significant work over 40 years on water splitting, the actual efficiencies reported for a wide variety of photocatalytic systems are still far from a technologically feasible situation for solar hydrogen production.[2] To date, the best performance has been obtained by TiO_2 based systems using UV light. In spite of that, this is of great importance for solar applications. Although UV region constitutes a small fraction of solar spectrum, the high efficiency of this UV photogenerated carriers justifies the studies at lab scale and would be the basis for pilot plant scaling-up.[3]

However, some important factors make its application at present far from practical situation. The rapid recombination process of the photogenerated charge pairs and the occurrence of backward reactions are considered critical issues that hinder high efficiency.

Traditionally, many catalytic systems incorporate metal ions as charge trapping sites which can avoid the electron–hole recombination processes.[4] The most active metals are noble metals (Pt, Au, Ag, Pd, Rh)[5,6,7]. It has been found that the addition of these noble metals could have different effects on the photocatalytic activity which is also strongly affected not only by the nature of metal but also by other parameters including sample history and features of the metal.[8] Mul *et al* argued that the understanding of metallic particle sizes and its dispersion, the specific functionality of each co-catalyst is crucial for the development of active systems for hydrogen production.[8]

In this sense, Au and Ag show a surface plasmon resonance (SPR), which can absorb certain ranges of visible light that could improve the photocatalytic performance of TiO_2.[4,9] On the other hand, in the case of Pt, the enhancement in the photocatalytic activity is due to the Schottky junction formation at the interface between Pt and TiO_2, resulting in a larger barrier height with respect to Au and Ag nanoparticles.[10,11] This way the improvement in the photocatalytic activity could be due by the hindering of the electron–hole (e^-–h^+) recombination rate.

Alternatively, transition metal doping with Cu, Fe, Co or Ni have been proposed as a promising cheaper option in comparison to noble metals. However, the efficiencies showed are still low in comparison to noble metals.[3,12,13]

Moreover, as reported in many other catalytic processes, significant activity improvement is usually obtained by formulations containing bimetallic components.[14,15] This is due to their higher tunability with respect to monometallic systems. Thus, according to metals features, bimetallic active sites can show different structures, metal(s) support interactions, etc. Moreover, the structure of bimetallic clusters can varied from bimetallic hetero-structures, to core–shells, alloyed clusters, changing each case the type of metal interaction. In addition, the modification of a metal oxide such as TiO_2 with bimetallic nanoparticles could be also a feasible strategy for enhancing hydrogen generation, at the same time minimizing the use of expensive noble metals. Among the improvements achieved by the bimetallic formulation, we may highlight the formation of unique interfaces at metal–support and metal–metal heterojunction that may increase the stability and enhance the interfacial charge transfer kinetics.[16] In the case of photoreforming reaction, an improved co-catalyst stability would certainly affect to the final H_2 production.

Many examples have been reported in the literature describing improvements using bimetallic co-catalysts compared to monometallic ones. Thus, Murcia *et al* proposed bimetallic Cu-Ag and Cu-Pt co-catalytic systems showing higher H_2 productivities, where the presence of Cu aids the control of the extent of the oxidation reaction.[17] Similarly, bimetallic Pd-Ni samples have been reported to be more efficient than either monometallic systems. These authors reported a synergetic effect with the presence of Pd nanoparticles and Ni^0-NiO clusters on TiO_2.[18] An enhanced rate of hydrogen evolution was obtained for Au-Ni co-modified TiO_2, revealing a synergetic effect of the two metals.[19] The evidence so far is that the role of the metal is not only to avoid the recombination of charge-carriers by trapping electrons[4], but also to act as a recombination center for atomic hydrogen (H·) from water oxidation or alcohol reforming to produce hydrogen.

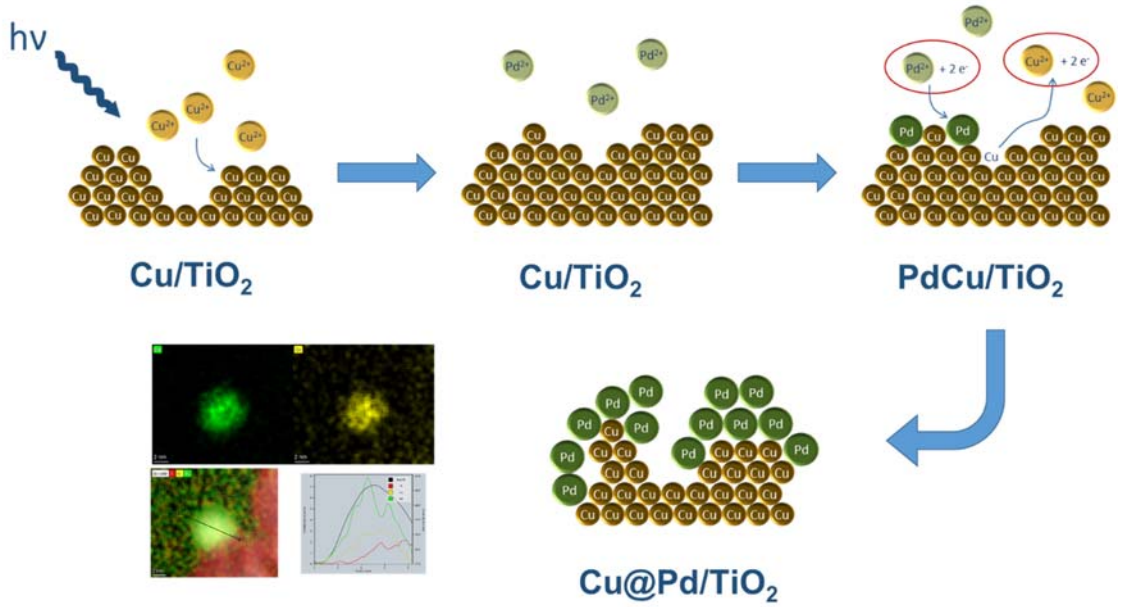
In the present paper we present an interesting approach to copper based catalysts by incorporating increasing amounts of palladium into a bimetallic or core-shell structure supported on TiO_2. The proposed preparation method through redox displacement assure the selective location of these palladium atoms intimately joined to copper. In fact, redox displacement has been reported as a very effective method for the preparation of core-shell materials.[20] Thus core-shell structuration of Pd clusters supported on TiO_2 induces a notable improvement of the photoreforming behaviour of monometallic Pd/TiO_2 system to produce hydrogen.

EXPERIMENTAL

Catalysts preparation and characterisation

The TiO_2 system used in the present work was commercial Evonik P25. Then metal loading was performed through sequential deposition procedure (**Scheme 1**). At a first

step, copper was deposited by photodeposition method using a close immersion-well reactor. In this case, 0.5 g of TiO_2 was suspended in 350 mL of isopropanol-water (1:10 v/v) containing the stoichiometric amount of Cu^{2+} precursor for a nominal loading of 2 at%. Photodeposition was achieved by illumination with UV lamp (125 W medium pressure Hg lamp) under N_2 flow (20 mL/min) for 1 hour at 18ºC ± 1ºC. After that, lamp was switched off and the stoichiometric amount of Pd^{2+} was added to the above suspension (from 0.05 at% to 1.0 at%). This mixture was stirring in the dark for 1 hour at the same temperature and N_2 flow. At this moment, Pd^{2+} ions were interchanged with deposited Cu^0 atoms through galvanic replacement process.[20] Therefore, initial Cu^{2+} content would vary as a function of Pd^{2+} incorporated. The obtained systems were filtered, thoroughly washed with distilled water and finally dried at 90 ºC. Bimetallic doped systems are expected to have 2 at% loading and were denoted as Cu@Pd_y, being *y* the Pd at%. Monometallic Pd systems were prepared by photodeposition method as in the case of monometallic Cu.



Scheme 1: Multistep preparation synthetic route for core-shell structuration through galvanic replacement.

BET surface area measurements were carried out by N_2 adsorption using a Micromeritics 2000 instrument.

X-ray diffraction (XRD) patterns were obtained using a Siemens D-501 diffractometer with Ni filter and graphite monochromator. The X-ray source was Cu Kα radiation. From the line broadening of corresponding X-ray diffraction peaks, we have calculated the anatase fraction as well the mean crystallite size by Rietveld fitting using HighScore-Plus software.

Inductively coupled plasma-optical emission spectroscopy (ICP-OES, iCAP 7200 Duo, ThermoFisher Scientific) was applied to determine the metal loadings in the samples. Samples were previously dissolved by means of acid digestion with a H_2SO_4 and H_2O_2 mixture.

Diffuse reflectance spectra were obtained on a UV–vis scanning spectrophotometer Agilent Cary 300, equipped with an integrating sphere, using Spectralon® as reference material. UV-vis spectra were performed in the diffuse reflectance mode (R) and transformed to a magnitude proportional to the extinction coefficient (K) through the Kubelka-Munk function, $F(R_\infty)$. For the sake of comparison, all spectra were arbitrary normalized in intensity to 1. Band gap values were obtained from the plot of the modified Kubelka-Munk function $(F(R_\infty)E)^{1/2}$ versus the energy of the absorbed light E.

The morphology of samples was followed by means of TEM microscopy (JEOL 2100Plus microscope). The samples were dispersed in ethanol using an ultrasonicator and dropped on a nickel grid. High-angle annular dark field scanning TEM (HAADF-STEM) images and energy-dispersive X-ray (EDX) elemental maps were performed using a TALOS

F200S microscope from FEI company, working at 200 kV with 0.25 nm resolution, with a Super-X: 2SDD EDX and HAADF-STEM detectors. The samples were deposited on a holey carbon support film on 400 mesh Au grid, without using any solvent to avoid contamination during the maps acquisition. Field emission scanning electron microscopy (SEM-FEG) was performed by using a Hitachi S4800 microscope. In this case, the samples were dispersed in ethanol using an ultrasonicator and dropped on a nickel grid.

XPS data were recorded on pellets prepared by slightly pressing the powdered materials which were outgassed in the prechamber of the instrument at room temperature up to a pressure < $2 \cdot 10^{-8}$ torr to remove chemisorbed water from their surfaces. Spectra were recorded using a Leybold-Heraeus LHS-10 spectrometer, working with constant pass energy of 50 eV. The spectrometer main chamber, working at a pressure <$2 \cdot 10^{-9}$ Torr, is equipped with an EA-200 MCD hemispherical electron analyser with a dual X-ray source working with Al *Kα* (hν = 1486.6 eV) at 120 W and 30 mA. C*1s* signal (284.6 eV) was used as internal energy reference in all the experiments.

Temperature programmed reduction (H_2-TPR) was performed using a Chemstar instrument (Quantachrome). About 80 mg of the catalysts previously degassed at 120 °C for 30 min under Ar flow. The TPR spectra were collected in 10 mL/min mixture of 5% H_2/Ar from 35 ºC to 700 °C with a heating rate of 10 °C/min.

CO adsorption on the fresh catalysts (pretreated in He at 120 ºC for 30 min) was performed in a Harricks praying mantis cell. The spectra were recorded on a Nicolet FT-IR spectrometer at 50 ºC with a resolution of 4 cm^{-1}. After pretreatment, samples were exposed to CO/He flow for 10 min. Then, spectra were recorded after evacuated with He for 10 min. The contribution from CO in the gas phase was in all cases eliminated by subtracting the corresponding spectra obtained from the bare TiO_2 support.

Photocatalytic runs

Photocatalytic H_2 production tests were performed in a flow-reactor system (**Figure S1**). The powder photocatalysts were suspended in water-isopropanol solution (1:9 v/v). The reaction media was continuously thermostated at 18ºC ± 1ºC to prevent any temperature effect. The catalyst suspension (0.5 g/L) was firstly degassed with an N_2 stream (80 mL/min) for 30 min to remove dissolved and headspace oxygen. After that the N_2 flow was settled at 15 mL/min and stabilised for 30 min. This nitrogen flow was used to displace the hydrogen produced from the photoreactor headspace towards the GC measuring system. Then, the lamp (125 W medium pressure Hg lamp) was switched on and the effluent gases were analysed to quantify H_2 production by gas chromatography (Agilent 7890B GC) using a thermal conductivity detector. The photonic efficiency for the H_2 evolution reaction has been determined from the reaction rate and the flux of incoming photons (calculated for the irradiation wavelengths of 365 nm)[13]. In order to determine the intermediates originated during isopropanol photoreforming, we have also performed the qualitative analysis of the liquid phase by GC-MS (Agilent 7000D).

Computational Methodology

All density functional theory computations presented are carried out in a periodic plane wave basis set using the VASP.5.4 code.[21] The cut-off for the kinetic energy is 400 eV and projector augmented wave all-electron, frozen core potentials[22] are used, with the following valance electron configurations: Ti $4s^2\ 3d^2$, O $2s^2\ 2p^4$, Cu $4s^1\ 3d^{10}$, Pd $4d^{10}$ and the one-electron hydrogen PAW potential. The Perdew-Wang 91 approximation to the exchange-correlation functional is used.[23] The bulk lattice parameters for rutile were computed as a=b=4.614 Å and c=2.962 Å The TiO_2 substrate is the (110) rutile surface,

with a (4x2) surface supercell. This slab has 6 O-Ti-O trilayers and no dipole. The vacuum region is 12 Å.

The convergence criteria for the energy and forces were 10^{-4} eV and 0.02 eV $Å^{-2}$, respectively. The k-points were sampled at the Γ-point and aspherical gradient corrections were applied throughout. Gaussian smearing with σ = 0.1 eV and the Methfessel-Paxton smearing method was used.

A Hubbard U correction[24] was applied to the Ti *3d* states with U(Ti) = 4.5 eV, consistent with previous work.[25,26] This correction is necessary in describing the partially filled d-orbital and reduced Ti^{3+} states.[27]

RESULTS AND DISCUSSIONS

Photocatalytic Reforming on Cu@Pd/TiO_2 systems.

In **Figure 1** we show the evolution of H_2 production from isopropanol over time for different catalysts. For monometallic Pd systems (**Fig. 1.a**) the H_2 production rates showed a drastic diminution upon the first 30 minutes (not shown), leading to a visible decay curve in the H_2 production upon time. From the evolution of H_2 yield, the maximum production is attained for $Pd_{0.3}$ sample. If we consider the bimetallic systems (**Fig 1.a**), it is clear that copper promotes a stabilization effect in H_2 production over time and a more linear production of H_2 curve can be observed for Cu@Pd systems. This shows less diminution in H_2 production rates and therefore less initial deactivation.

Different factors would be the responsible of this important diminution of reaction rate. Similar deactivation of the photocatalysts has been also reported for Pt/TiO_2 systems and was explained by considering a strong metal-support interaction between the noble metal and TiO_2.[28] Strong metal–support interactions (SMSI), have been frequently discussed as

a major source of deactivation in heterogeneous catalysis for noble metals supported on metal oxides.[29,30] Furthermore, it is well-known that similar to platinum, Pd supported TiO_2 also shows a marked SMSI effect. In this sense, Haselmann *et al* observed metal encapsulation by TiO_2 which leads to the early-stage deactivation during the photoreforming reaction.[28] Thus, upon reaction Pd active sites would be progressively encapsulated by in situ formed Ti^{3+} leading to the deactivation of the noble metal.

At the same time, metal clusters could suffer aggregation during the reaction. Thus, initial high photoactivity due to small metal size would decay as aggregation become important.[31,32] Indeed, these authors argued that core-shell structuration would favour the size stability.[33]

As a result, the resulting decrease in accessible active surface area would be responsible for a partial loss of catalytic activity. In addition to this possible deactivation route, the formation at the first stage of the reaction of certain intermediates from the sacrificial agent would also induce the loss of activity.[28]

In this sense, in **Table S1** we summarize the intermediate detected in the liquid phase after 5 hours of reaction. Only acetone and pinacol (*2,3-dimethyl-2,3-butanediol*) were detected in the liquid phase. Acetone was formed from the first stage of the reaction, being important for $Pd_{1.0}$ sample. In this case, it is observed that the amount of acetone slightly decays with time after the fourth hour of reaction. Pinacol is also observed along the reaction period. Acetone and pinacol follow similar trend and as acetone start to diminish, pinacol presence also decays. This is effect can be correlated to the drastic diminution of H_2 production after this initial period. In the case of $Cu_{2.0}$ sample, acetone shows a progressively growth along the first 5 hours while pinacol starts to appear after the third hour. $Pd_{1.0}Cu$ sample shows an intermediate behavior, acetone evolution is similar as for $Cu_{2.0}$ however pinacol is formed just from the beginning as occurred for $Pd_{1.0}$

photocatalyst and at similar extent. From these results, it can be inferred that the presence of pinacol cannot be related to the catalyst deactivation. The evolution of different intermediates in the liquid phase directly reflect the extent of the reaction for each catalyst and also the different nature of active sites.

Even more, photocorrosion of active sites have been also claimed as a factor determining the stability of the photocatalysts upon H_2 photoreforming. Particularly for Cu doped photocatalysts, Toe *et al* proposed simultaneous occurrence of self-photoreduction and photooxidation of Cu^+ active sites.[34] This fact would occur when a high e^- consumption rate for H_2 generation is not accompanied by the same rate oxidation of the sacrificial agent, thus excess of photogenerated h^+ would promote active site oxidation.

On this basis, in **Table S2** we summarized the efficiencies at mid-term and long-term reaction times, (5 and 18 hours respectively). For both monometallic and bimetallic series, the lower AQE observed for long reaction time would point out the progressive deactivation of the catalysts as already mentioned. For monometallic palladium systems, apparent efficiencies at 18 hours are notably lower than those after 5 hours (AQE 7.87 vs 4.00 respectively in the case of $Pd_{1.0}$), denoting a progressive deactivation of the catalysts. In a much less extent, monometallic copper catalyst also showed certain diminution of the photocatalytic efficiency after 18 hours (AQE 4.14 vs 2.95 respectively).

Interestingly, bimetallic systems show a quite different behavior. At mid-term reaction times, those systems give lower efficiencies with respect to the same nominal Pd/TiO_2 system when palladium is below 0.5 at%. Thus, only in the case of $Pd_{1.0}Cu$ samples the apparent efficiency is significantly higher than for the corresponding monometallic Pd samples, showing a composite effect. Moreover, for long-time experiments it is worthy to note that Cu@Pd bimetallic systems exhibit clearly higher AQE values with respect to

the corresponding Pd monometallic one. Thus, a clear stabilization in the catalyst performance could be proposed.

If we consider the total H_2 produced after 18 hours (**Figure 1.b**) we can see that for monometallic Pd samples a maximum H_2 yield is attained for $Pd_{0.3}$ sample. The evolution of H_2 yield for Cu@Pd bimetallic systems is more complex. As expected, as Pd is incorporated the total amount of H_2 produced is increasing. However, for intermediate Pd contents it seems that a plateau is achieved just around the maximum for monometallic Pd systems. Thus, it can be said that bimetallic Cu@Pd catalysts could behaving as the corresponding monometallic catalyst. However, for higher Pd content the total H_2 produced is markedly higher than those obtained for monometallic Pd.

On this basis, we could state that the deactivation observed for higher metal content Pd/TiO_2 is suppressed for the bimetallic systems. From these results, we could tentatively suggest that the presence of Cu in the bimetallic photocatalyst would avoid or mitigate against the occurrence of a tentative SMSI effect or even the aggregation of metal clusters. This leads to a significant stabilization of the photocatalytic activity over time. In addition, palladium would avoid the possible copper photocorrosion. Thus, when palladium is introduced at 0.5 at% the H_2 yield is ca. 350 mmol/g after 18 hours (30% more than that obtained for a monometallic $Pd_{0.5}$ sample).

It is quite complicated to make a direct comparison in H_2 yield with other reported systems since this value is highly affected by operational conditions such as reactor geometry, lamp power and light nature, sacrificial agent or catalyst concentration. However, a simple correlation with similar isopropanol photoreforming experiments in the literature clearly shows that our bimetallic system would show a better performance than other noble metal monometallic ones. Thus, Velazquez et al reported the effect of reaction temperature and sacrificial agent on the photocatalytic H_2-production over Pt-

TiO_2 catalyst. In this case, using a similar reactor and a 300 W Hg lamp, the optimum H_2 production with isopropanol as scavenger was 9.4 mmol/g·h.[35], being notably lower than that obtained in the present work. Al-Azri et al also reported the H_2 production using different alcohols as hole scavengers over Pd/TiO_2 catalysts.[36] When using isopropanol as scavenger and 1 wt% Pd/TiO_2 catalyst, the H_2 yield was 17 mmol/g·h, slightly lower than our best value obtained with $Pd_{1.0}Cu$ catalyst (350 mmol/g after 18 hours, which represents an average 19 mmol/g·h along a long reaction time).

Structural, Surface and Electronic Characterization of Cu@Pd/TiO_2 systems.

In order to understand the particular behaviour of supported Cu@Pd bimetallic catalysts with respect to the monometallic catalyst, a range of characterization approaches has been explored. As mentioned before, the incorporation of Pd would be achieved by a redox displacement process of the former photodeposited copper. The effectiveness of the sequential metal deposition has been corroborated by ICP chemical analysis (**Table S3**). Copper and palladium monometallic systems showed metal concentrations very close to the nominal ones (2.12 and 1.03 at% respectively). For the bimetallic systems, it is clear that upon addition of Pd^{2+} a redox displacement takes place and palladium progressively replaces Cu^0 from the surface. The chemical analysis also reveals that while palladium content is in all samples close to the nominal value, copper loading is quite lower than the expected nominal loading (**Figure S2**). Therefore, in the displacement redox reaction one palladium ion is moving more than one copper ion. This could be explained by considering that copper is not fully reduced after the photodeposition step. From these results, it is worthy to point out that contrary to what might be expected, $Cu@Pd_{1.0}$ sample is mainly constituted by Pd, with a small residue of copper (0.3 at%). This is particular interesting if we recall the important effect of this small fraction of copper on the photocatalytic hydrogen evolution at mid-term reaction time as shown in **Table S2**.

The X-ray diffraction patterns of the metal-TiO_2 systems are shown in **Figure S3.a**. As it is well-known, TiO_2 P25 powders consist of a mixture of anatase and rutile phases (JCPDS 89-4921 and 75-1756, respectively), with 85-88% anatase phase from Rietveld fitting. Photodeposition of Cu and Pd does not produce any effect in the crystalline structure of TiO_2, suggesting that they are not doped into the TiO_2 crystal structure Moreover, the subsequent redox replacement procedure does not alter either the phase composition or crystallite size of TiO_2. Due to the low loading and the high dispersion of the metallic clusters, monometallic Cu and Cu-Pd species are not detectable from this technique. Only in the case of $Pd_{1.0}$ sample it is possible to envisage a small and broad diffraction peak at ca. $2\theta = 40^{o}$ which would be assigned to Pd (111). This could indicate that in spite of the low Pd content, the cluster size is large enough to induce the appearance of this tiny diffraction peak. Similarly, the surface area was not affected by the deposition procedures of the metals (**Figure S3.b**) with at most a slight decrease of surface area when the metals are deposited onto the TiO_2 surface. Thus, the specific surface area measured correlates with the reported value for commercial TiO_2 P25, being in all cases 50 $m^2/g \pm 2$ m^2/g.

The morphology of the deposited co-catalysts has been studied by TEM microscopy (**Figure 2, 3 and S4**). TiO_2 P25 consists on well-defined roundish particles of about 20-30 nm, which is in agreement with the crystallite size calculated from XRD (**Table S4**). After Cu photodeposition, small deposits can be noticed on some TiO_2 particles (**Figure 2.a**). Such small copper clusters would show 2-3 nm size. On the other hand, photodeposited Pd clusters appear homogeneously distributed on the TiO_2 surface showing a narrow size distribution around 4 nm (**Figure 2.b**). As Pd is incorporated the metal clusters became more obvious arising from the reduced character of the metal deposits (**Figure S4**). Moreover, the average particle size progressively increases from

ca. 2 nm to 4 nm as Pd is incorporated. In addition to this size growth, there is increased aggregation of the particles for higher Pd content (**Figure 2.c**). Indeed, $Cu@Pd_{1.0}$ sample mainly shows this aggregate morphology. The core–shell structure of the proposed Cu@Pd NPs was verified by STEM-EDS. **Figure 3** shows a HAADF-STEM image of $Cu@Pd_{0.3}$. From selected EDS elemental mapping along corresponding line-scan plot it is evident that Cu nanoparticles are confined in the center of the nanoparticle while Pd appears uniformly distributed throughout the entire particle. Thus, the EDS line-scan profile clearly evidences the core–shell structure of Cu@Pd nanoparticles. Moreover, in this side view of the nanoparticle, it is also evidenced that Cu is specifically in contact with Ti. We have observed a similar core-shell structuration for $Cu@Pd_{0.4}/TiO_2$ sample (not shown), denoting that the preparation procedure assure such morphology. Isolated Cu or Pd particles were not detected.

In order to assess any possible change of metal site morphology during the reaction, we have observed by TEM the $Cu@Pd_{1.0}$ and $Pd_{1.0}$ samples after 5 hours of reaction (**Figure S5**). It is worthy to note that $Pd_{1.0}$ clearly suffers an important cluster size growth, showing an average particle size of 5.6 nm. However, $Cu@Pd_{1.0}$ seems to loss the aggregated morphology, maintaining at the same time the cluster size (ca. 4.1 nm in this case). By comparing the average metal size for fresh and used samples, it can be clearly stated that $Pd_{1.0}$ sample shows an important size growth in the first 5 hours of reaction (5.6 nm vs 4.0 nm for used and fresh samples respectively). The behavior of bimetallic system is completely different. In this case, the initial Pd aggregates seems to diffuse on TiO_2 support surface keeping the metal cluster size. In this sense, Spanu et al observed from operando XAS study the dissolution/redeposition process in a $CuNi/TiO_2$ catalyst under UV illumination.[37] These authors argued that partially oxidized Ni and Cu present in the catalyst would be dissolved during reaction that would be further reduced/redeposited as

a bimetallic NiCu phase at the TiO_2 surface under illumination. This complex mechanism would explain the aggregation observed in Pd monometallic systems and the stability of bimetallic ones at long reaction times.

We also mention that attending on examining the evolution of the Pd and Cu content from ICP chemical analysis, for Pd contents higher than 0.4, the amount of copper appears to be stable. Therefore at higher Pd loadings, copper can still reduce Pd but without being displaced. The complete coverage of copper clusters by palladium at this Pd content would block further displacement of copper. Thus, palladium reduction and deposition over metal clusters would proceed without copper leaching. Upon this situation, the electron transfer from copper core to palladium in solution would take place through the metallic palladium shell or even through TiO_2 support. We would consider that Cu photodeposition take place over defective points of TiO_2. At this defective structural points electron transfer would be favoured and would allow Pd^{2+} reduction and deposition.

We have also measured the UV−vis DRS to study the optical properties of photocatalysts. **Figure S6** shows the diffuse reflectance spectra for different Cu@Pd/TiO_2 systems. The strong absorption band below 380 nm (giving a band gap value of 3.2 eV) would correspond to the ligand to metal $O^{2-}\rightarrow Ti^{4+}$ charge transfer (LMCT) transitions in the TiO_2 support. In addition, new absorption bands can be observed in the visible range for all systems. As reported in the literature, CuOx generally exhibits absorption bands in the visible range at 400-600 nm and above 700 nm, assigned to both Cu^+ and Cu^{2+} species.[38,39] $Cu_{2.0}/TiO_2$ shows a small shoulder at 450 nm and broad band at around 780 nm. The absorption edge for Cu_2O nanoparticles corresponding to an interband transition has been located at ca. 441 nm.[40] Moreover, the absorption at wavelengths than 650 nm would be consistent with the intraband absorption of Cu_2O NPs.[40,41] This later band would extent

to 700-800 nm range and can be understood in terms of d–d transition of copper ions. Metallic copper is reported to show a plasmon resonance absorption between 450-600 nm which strongly depends on the cluster size.[41,42] Therefore the likely coexistence of Cu^0 and Cu^+ species can be derived from the UV-vis absorption spectrum.

The occurrence of Pd ions in the bimetallic systems, even at low content, results in an intense absorption in the visible region. Indeed, the absorption at around 460 nm has been associated to the *d-d* transitions of Pd^{2+} ions from the energy states of –O–Pd–O– surface species to the TiO_2 conduction band.[43] Furthermore, metallic Pd also shows a plasmon absorption (surface plasmon resonance effect) at around 500 nm.[44] However, a further increase of the Pd loading leads to an excessive absorption which is caused by the induced light scattering phenomena which restricts a clear interpretation of the present species.

To further clarify the nature of the surface Cu and Pd species we have performed FTIR analysis of CO chemisorption and TPR analysis (**Figure S7**). The infrared spectrum of irreversibly adsorbed carbon monoxide for $Cu_{2.0}$ TiO_2 sample presents intense bands located at 2110 and 2095 cm^{-1} and an additional smaller band at 2055 cm^{-1} (**Figure S7.a**). It has been reported that CO adsorption onto copper showing different oxidation states leads to absorption bands located between 2050 and 2220 cm^{-1} according to the crystal plane and to the nature of the support.[45] Previous literature studies of CO adsorption yield the following assignments: bands in the range 2220−2150 cm^{-1} have been associated to Cu^{2+}–CO, whereas bands in the range 2160−2080 cm^{-1} are attributed to Cu^+–CO. Metallic copper carbonyls, which can be single-site or nanostructures species are expected to be located below 2130 cm^{-1}.[46,47] Due to the overlapping of different Cu species, the interpretation of CO adsorption by FTIR is quite complex. Nevertheless, as a general trend, it is widely accepted that that peaks >2100 cm^{-1} could be ascribed to CO adsorption on oxidized copper species Cu^{n+}, while peaks <2100 cm^{-1} are due to CO

adsorption on metallic copper.[48] Therefore, at the first glance, since no signal has been observed at wavenumber higher than 2110 cm^{-1}, the first important statement would be the lack of Cu^{2+} species. This fact will be discussed later. Moreover, considering the above assignments from other works, we could propose that more intense bands at ca. 2110 cm^{-1} with its shoulder at 2095 cm^{-1} observed in the present work could be assigned to edge sites or Cu^{+} species and linearly adsorbed CO onto metallic copper at edge or corner sites, respectively. In addition, the small band at 2055 cm^{-1} could be ascribed to the adsorption onto Cu (111) facet of small metallic copper particles.

On the other hand, monometallic Pd/TiO_2 system shows two absorption bands for irreversibly adsorbed CO. A broad band centered at around 1980 cm^{-1} (with poorly resolved shoulders at 1985 and 1950 cm^{-1}), corresponds to bridged multicentered carbon monoxide.[49] An additional small wide band at 2065 cm^{-1} has been associated to carbon monoxide bonded to surface palladium atoms in linear forms.[49,50] The band at about 1980 cm^{-1} is notably stronger than that at 2065 cm^{-1} and this is due to the larger particle size of Pd which favours multibridged CO adsorption. It has been discussed that CO adsorption on Pd^{2+} and Pd^{+} results in bands at 2173 cm^{-1} and 2120 cm^{-1}.[51] In our case the absence of bands at such wavenumbers would clearly demonstrate that only metallic Pd is present, as it would be expected from photodeposition method.

Thus, considering these assignments for monometallic systems, describing the CO IR absorption bands for bimetallic one becomes quite complex.

For low Pd content we observe the following evolution in the FTIR bands: i) the 2095 cm^{-1} band trends to disappear as Pd content increases; ii) the overall intensity of the originally intense band 2110-2095 cm^{-1} progressively diminishes and is shifted to 2105 cm^{-1}; iii) the band at 2055 cm^{-1} remains almost unaltered for low Pd content; iv) a new broad band at 1985 cm^{-1} starts to develop. This evolution clearly shows that the addition

of Pd will diminish the bands corresponding to CO adsorption at Cu^{+},Cu^{0}. Moreover, such diminution seems to be more evident for the band at 2095 cm^{-1}, that has been formerly assigned to metallic copper at defective sites. In addition, a progressive shift toward lower wavenumber would indicate that the remaining copper is strongly affected by the presence of palladium. From the evolution of the bands formerly assigned to copper (Cu^{+} and/or Cu^{0}) we would envisage two important processes: i) the loss of copper from the surface; ii) covering of copper by Pd. Thus, it can be concluded that Pd^{2+} tends to replace Cu^{+} and Cu^{0} located at defective sites in the cluster. Moreover, as the Pd content increases, the band at 2055 cm^{-1} previously associated to linearly bonded CO seems to be also affected. Additionally, the occurrence of a new wide band at 1985 cm^{-1} for Pd contents higher than 0.1 mol% would indicate the presence of metallic Pd species multicentere bonded with CO. Therefore, it is clear that the incorporation of Pd^{2+} into the surface is taking place as metallic palladium due to a redox replacement process. As in the case of monometallic Pd systems the greater intensity shown by the band at 1985 cm^{-1} would indicate the larger size of Pd clusters. From these considerations, it can be envisaged that palladium incorporation would take place intimately at copper clusters, in good agreement with STEM analysis (**Figure 3**).

The copper-palladium interaction can be examined by analyzing the reduction behavior of the metal clusters by H_2 temperature programmed reduction (**Figure S7.b**). The TPR profile of the reference $Cu_{2.0}$ sample exhibits a three step H_2-consumption at 130 ºC, 150 ºC and 168 ºC corresponding to reduction of $Cu^{2+/+}$ species to metallic copper. From the H_2 consumption and taking into account the consumption for a CuO reference, we calculate that the metal loading corresponds to 2.1 at%, which is close to the nominal value from ICP. This would indicate that whole Cu^{2+} in the solution has been photodeposited, which is also in agreement with ICP analysis (**Table S3**), and that a 2+

oxidation state is present. This could appear to contradict the previous information drawn from FTIR. Indeed, from CO adsorption it was stated that no Cu^{2+} is present in Cu/TiO_2. This could be explained by the easy reducibility of Cu^{2+} species. Thus it could be said that Cu^{2+} would be rapidly reduced to Cu^{+}/Cu^{0} in the presence of CO. In fact, the lower reduction temperatures would point out the easy reduction of any Cu^{2+} species to Cu^{0}, probably due to the high dispersion (which include isolated copper ions, weak magnetic associates, and small two- and three-dimensional clusters) as well the soft interaction with TiO_2 support. Indeed, we have previously shown from DFT studies that the reduction of CuO (111) with H_2 is favourable.[52]

In the case of the $Pd_{1.0}$ sample, two significant effects can be observed. Firstly, a negative H_2 consumption peak at around 77 °C is ascribed to H_2 release from palladium hydride β-PdH_x.[53] This palladium hydride was formed during H_2 purge and TCD stabilization prior to TPR analysis. Thus, H_2 could be absorbed by metastable Pd crystallite particles at ambient temperature. A second effect is observed at around 340 ºC which would be either assigned to the hydrogen consumption by a spillover from Pd to the support material,[54] or to the reduction of oxidised PdOx species in intimate contact with the support.

For bimetallic systems, the former reduction peak of copper shows two important effects. The H_2 consumption peak is shifted to lower temperatures (below 100 ºC), and this shift is more notable as the Pd content increased. Besides, H_2-TPR peaks show markedly reduced intensities. These two effects would indicate out that reduction process of Cu species is taking place at lower temperature, probably due to the strong interaction with Pd. Such a promotion in the CuO_x redox potential should be the result of a SMSI effect between Pd and CuOx that facilitated the diffusion of dissociated hydrogen to Cu clusters.[55] Thus, the formation of bimetallic clusters can be envisaged. Secondly, the

lower intensities for H_2-TPR peak could be explained by considering the negative peak exhibited by Pd corresponding to the H_2 desorption from β-PdH_x species. Given that these two effects, Cu reduction uptake and Pd desorption release, are observed at similar temperatures, they could be partially balanced leading to a significantly supressed H_2-TPR peak. Moreover, Batista *et al* investigated the reduction of monometallic palladium, copper and bimetallic Pd–Cu catalysts and found that in the presence of palladium, Cu^{2+} would be reduced to Cu^0 at lower temperatures through a spillover mechanism.[56] Therefore, Cu would be partially reduced before TPR experiment leading to a lower H_2 consumption. The progressive diminution of the copper content would also lead to a lower H_2-TPR peak.

In addition to this small reduction peak, further H_2-uptake is found at around 340 ºC which is unaltered with Pd content. This, second reduction peaks was already present in $Pd_{1.0}$ TiO_2 sample so the occurrence might be associated to the presence of Pd in the bimetallic system. As in the case of monometallic system, this peak could be associated to the reduction of a small fraction of PdOx as well as reduction of the TiO_2 support through spillover process.

Surface features of Cu@Pd/TiO_2 systems have been also studied by XPS. In **Figure 4** (*upper row*) we show the Cu *2p* and Pd *3d* XPS peaks for all systems. Firstly, it can be said the all bimetallic systems show the presence of both doping ions denoting that the replacement of Cu by Pd has been successful. Thus, as we increased the amount of Pd it is evident that Cu content is progressively decreased (**Table S3**). It is worthy to note that the evolution of surface composition attained from XPS is similar to that obtained from chemical analysis.

To evaluate the oxidation states of Cu and Pd species deposited on the TiO_2 support, we measured the Cu $2p_{3/2}$ and Pd $3d_{5/2}$ electronic transitions, as well as the Cu LMM Auger

transitions. Considering the Cu *2p* level (**Figure 4.a***, upper row*), there is a clear doublet located at 934.2 and 952.1 eV. From the binding energy value and the absence of the shake-up satellite we can state that copper species are Cu^0 and/or Cu^+, which agrees with CO-FTIR discussion. Similarly, the easy reducibility of former Cu^{2+} species, would favour the occurrence of reduced Cu^+/Cu^0 species during XPS analysis. Attending to the Cu *LMM* auger transition (**Figure 4.b***, upper row*) it is possible to assess that a mixture of Cu^0 and Cu^+ is always present.[57] From the relative intensities of Cu *LMM* peaks at kinetic energies ca. 917 and 919 eV (from this KE, modified Auger parameters of ca. 1849 end 1851 eV can be attained), which correspond to Cu^0 and Cu^+ respectively, we could estimate the Cu^0/Cu^+ ratio in the different systems (**Table S5**). Monometallic Cu/TiO_2 systems shows a mixture of Cu^0 and Cu^+, with Cu^0 being the predominant oxidation state. As Pd is incorporated the amount of Cu^0 significantly increases. On the other hand, the considering Pd *3d* peak, it can be noticed that it is composed by three peaks located at ca. 334.5 and 336.5 eV which correspond to Pd^0 and Pd^{2+} respectively (**Figure 4.c***, upper row*). The first important point that can be drawn is that for lower palladium loadings the binding energy values for Pd *3d* is notably positively shifted with respect to bare Pd sample (ca. 335.5 eV for $Pd_{0.2}Cu$ sample vs 334.6 eV for $Pd_{1.0}$ sample). This clearly denotes a possible electron transfer from Pd to Cu, and it confirms that for this lower palladium content systems, the electronic states of Pd were altered by the electronic interactions between Pd and Cu clusters. Similar positive shift in the Pd *3d* band has been already shown for Pd-Co as well as for Pd-Cu systems.[58,59]

By deconvoluting this peak it is possible to estimate the reduction degree of Pd species on the surface (**Table S5**. For the monometallic Pd system, practically the 80% consists on Pd^0. However, when Pd is incorporated with Cu, the amount of oxidized Pd increases. This trend can be related to the evolution of Cu species. As mentioned, the originally

photodeposited copper consists of a mixture of Cu^0 and Cu^+. However, as Pd is incorporated the fraction of Cu^+ gradually diminishes. This could mean that palladium replacement primary affects Cu^+ which are not able to reduce completely palladium ions. Then, as palladium addition is higher, copper mostly remains in the metallic state, while at the same time the reduction degree of palladium is also higher. The higher reduced fraction of Pd together with the lower amount of copper would explain the lower H_2-TPR peak observed for Cu@Pd samples. From these considerations, bimetallic Cu@Pd system with intermediate compositions would exhibit a combination of metallic Cu and Pd which are present with some fraction of oxidised species. From combined interpretation of CO adsorption, TPR and XPS results it is possible to predict a strong interaction between incorporated palladium and copper which would support the idea that palladium is being deposited over copper clusters forming a core-shell structure at higher Pd content. This core-shell structuration have been also stated from TEM images.

If we represent the calculated Pd/Cu ratio from XPS versus Pd/Cu obtained from ICP (**Figure 4,** low*er row*), it is possible to note a tentative linear evolution for low palladium contents. However, for higher Pd loadings, Pd/Cu from XPS analysis appear above the theoretical Pd/Cu from ICP. This behaviour could indicate that, for higher contents, palladium is covering Cu clusters which remains buried. This fact has been previously stated from TEM images (**Figure 2**) for $Pd_{1.0}Cu$ sample for which aggregate clusters can be envisaged.

DFT Studies of Hydrogen Adsorption on Cu and Cu@Pd/TiO_2 systems.

DFT simulations of Cu, Pd and Cu@Pd modified model rutile TiO_2 (110) have been performed to explore the atomistic details of the activity towards H_2 production. **Figure 5** shows the atomic structure of our model systems, composed of a 1D periodic rod-like

structure of the metal (Cu or Pd) supported on a perfect rutile (110) surface; a similar model was used by Koga *et al* in their investigation of CO oxidation on Au-modified TiO_2.[60,61] This structure is then modified as follows: (1) substituting a small concentration (2.5%) of Pd in the outermost Cu layer; (2) a core-shell bimetallic structure in which the outer layer of Cu is replaced by Pd. While there are clearly many ways to prepare these Cu@Pd models, those we use herein are representative of small Pd concentrations and a supported core-shell Cu@Pd structure.

In these model structures, the metal binds to the rutile (110) surface through formation of new interfacial Cu-O bonds, with typical Cu-O distances of 1.95 – 2.10 Å; for comparison Cu-O distances in CuO and Cu_2O are 1.95 and 1.86 Å. As a result of depositing the metal on the rutile substrate, there are distortions in the metal rod upon relaxation. Typically, there are strong distortions in the Cu-Cu distances. In the interface region, these cluster around 2.45 – 2.58 Å (bulk Cu-Cu distances are 2.56 Å) or Cu-Cu bonds are broken, with typical Cu-Cu distances of 2.63 – 2.90 Å. In the regions away from the interface, typical Cu-Cu distances are 2.48 – 2.61 Å, which are moderately distorted from the bulk Cu-Cu distance. Clearly the interaction with oxygen on TiO_2 has a strong impact on the interface structure.

Introduction of a single Pd atom into the surface layer is 2 eV more stable than introducing Pd in the interface region. This has a notable effect on the local Cu-Pd distances, which are 2.55 – 2.69 Å and are elongated when compared to the corresponding Cu-Cu distances. In the interface region, the Cu-O distances are 1.98 – 2.25 Å. In the Pd-shell-Cu-core structure, Pd-Pd distances in the outermost layer are 2.60 – 2.75 Å, typical of the longer Pd-Pd distances compared to Cu-Cu distances. The Cu-Pd distances range from 2.45 – 2.61 Å, while the Cu-O distances in the interface are 2.05 – 2.26 Å.

Finally, for the pure Pd rod supported on rutile (110), the interface Pd-O distances are 2.08 – 2.26 Å, which is a shorter spread of distances than for Cu-O. Pd-Pd distances in the surface layer are 2.61 – 2.76 Å, consistent with the bulk Pd-Pd distance of 2.75 Å.

Given the preference for replacing Cu in the outermost layer with Pd, the formation of intimate Cu-Pd junction as a core-shell structure can be explained, corroborating the experimental results.

Thus, from the energetic point of view, the formation of intimate Cu-Pd junction as core-shell structure would be explained, corroborating the experimental results.

To understand how interface formation influences oxidation states of the metal and the TiO_2 surface we computed the Bader charges in the metal-TiO_2 systems, particularly focussing on those metal sites that are in the interfacial region and the influence of Pd incorporation. We also examine if Ti atoms in the support are reduced through charge transfer from the supported metal, a phenomenon that is well known for metals supported on metal oxides.[62,63,64] **Table S6** presents the computed Bader charges for the TiO_2-supported metallic rods.

The Bader charges of the interface Cu and Pd atoms show that the metal atoms that are in direct contact with the oxygen sites of TiO_2 are oxidised. The magnitude of the Bader charges on interfacial copper are consistent with a Cu^+ oxidation state.[65,66] The Cu atoms in the remainder of the structure, which do not interact with TiO_2, are metallic. This fact would be in agreement with XPS findings.

In the rutile (110) surface, three Ti atoms are reduced, with computed Bader charges of 1.66 and 1.72 electrons, which are consistent with formation of Ti^{3+} species. Ti^{4+} species have computed Bader charges of 1.28 electrons.

With a Pd rod supported on TiO_2, the interface Pd atoms are also partially oxidised and only two partially reduced Ti sites are produced in the TiO_2 support; these have computed

Bader charges of 1.39 and 1.42 electrons. Thus the extent of oxidation in Pd/TiO_2 is weaker than for Cu/TiO_2, which is related, in part, to the longer Pd-O distances.

In the Pd doped and core-shell structures, the computed Bader charges on Pd atoms that bind to copper are 16.28 electrons (single Pd atom) and in the range of 16.05 – 16.1 for the core-shell-like structure. This indicates Pd reduction upon replacement of Cu with Pd. The neighbouring Cu atoms are partially oxidised with computed Bader charges of 10.90 - 10.95 electrons for the single Pd atom and 10.7 – 10.90 electrons for the core-shell-like structure. These results showing Pd reduction and Cu oxidation are reasonable as Pd is more reducible than Cu, e.g. the standard reduction potential of Pd is +0.915 V and that of Cu is +0.337 V.

In understanding the experimental activity for hydrogen evolution (HER) with different compositions of Cu, Cu@Pd and Pd supported on TiO_2 we use as a descriptor the computed adsorption free energy of hydrogen atoms at the surface of the catalyst model.[67,68] This is the Volmer step in the HER, involving the adsorption of a proton and an electron at the catalyst. This step is then followed by either recombination of two adsorbed protons and electrons or interaction with a proton and electron from solution to produce H_2.

The ideal situation is that in which the adsorption free energy, ΔG_H, is ~0 eV. From the Sabatier principle, a free energy of adsorption of 0 eV means that the proton binds sufficiently strongly to undergo the next step, but not so strongly that it remains bound to the catalyst. For example, for Pt (111), the computed ΔG_H is *ca.* 0.09 eV, while for edge sites of MoS_2, it is 0.06 – 0.08 eV.[69,70] Given the uncertainties in DFT calculations of these energies, depending on functional, basis set and computational set-up, in this paper, we aim for computed Gibbs free energies of adsorption of +/- 0.15 eV to identify systems with suitable adsorption free energies of hydrogen.

Furthermore, we assess coverage effects through the simultaneous adsorption of two, four and five H atoms at the surface of the supported metal. Here we can determine the free energies of adsorption of *n* hydrogen atoms at metal-modified TiO_2, M/TiO_2, in one of two ways

(1) as an average, i.e. ΔG_H per adsorbed hydrogen (***Equation 1***):

$$\Delta GH/n = \{G(nH@M-TiO_2) - [G(M-TiO_2) + G(^{n}/_{2}\ H_2)]\}/n$$

(2) relative to *n-1* adsorbed hydrogen atoms (***Equation 2***):

$$\Delta\Delta GH = G(nH@M-TiO_2) - [G((n-1)H@M-TiO_2) + G(^{1}/_{2}\,H_2)]$$

In these equations, G(*n*H@M-TiO_2) is the computed adsorption free energy of *n* hydrogen atoms, G(*n-1*H@M-TiO_2) is the free energy of (*n-1*)H atoms, G(*n*H@M-TiO_2) is the free energy of *n* H atoms adsorbed at the surface of metal-supported TiO_2 and G(1/2H_2) is the free energy of hydrogen using half the DFT energy of a free H_2 molecule as the reference. The contributions of zero point energy and entropy at 300 K are computed as 0.25 eV, consistent with literature values.

Figure 6 shows the most favourable single hydrogen atom adsorption structures at the model metal-TiO_2 systems. We find single H atom adsorption modes with computed adsorption free energies that lie in the target range on all systems except the core-shell $Cu_{24}Pd_{18}$-TiO_2. For example ΔG_H = -0.03/-0.12 eV on Cu/TiO_2, ΔG_H = +0.04 eV on Pd/TiO_2 and ΔG_H = 0/-0.09 eV on $Cu_{41}Pd_1/TiO_2$. For $Cu_{24}Pd_{18}/TiO_2$ the closest adsorption energy is -0.22 eV. Where two energies are reported, this indicates two sites that meet the adsorption energy criterion at this hydrogen coverage.

These computed adsorption free energies indicate that, with the exception of the Cu@Pd core-shell structure, the metallic systems supported on rutile (110) have favourable adsorption free energies of hydrogen at this lowest coverage. The result for the core-shell

structure can be due to the presence of Pd sites that have Bader charges consistent with unoxidised or even partially reduced Pd in this surface layer and this promotes too strong adsorption of a low coverage of hydrogen. By contrast on the pure supported Pd rod, most of these atoms in the surface layer show Bader charges of 15.78 – 15.81 electrons that indicate partially oxidised Pd and this appears to moderate the strength of adsorption of hydrogen.

Considering the binding sites of the hydrogen atom, on all structures except Cu_{41}@Pd/TiO_2, this favourable binding site has a three-fold coordinated hydrogen atom. We now consider the role of coverage of hydrogen on the computed adsorption free energies. The atomic structures for favourable hydrogen adsorption free energies for the adsorption of up to five hydrogen atoms on Cu/TiO_2, Pd/TiO_2, 1PdCu/TiO_2 and core-shell Cu@Pd/TiO_2 are shown in Figures **7, 8, 9,** and **10,** respectively.

On Cu/TiO_2 the adsorption structures for two H atoms are shown in **Figures 7 (a)** and **(b)** and the average hydrogen free adsorption energies, ***Equation 1***, are -0.15 and -0.21 eV per H atom. These are at extreme of the energy range where H adsorption can be considered favourable. If we consider the adsorption free energy of the second hydrogen atom, given an adsorbed hydrogen atom, $\Delta\Delta G_H$ ***Equation 2***, then the computed adsorption free energies are -0.26 and -0.19 eV per H atom. Other H adsorption structures have computed adsorption free energies around -0.3 eV per H atom, suggesting that at this coverage of H atoms the binding to Cu is too strong to promote HER and H will be simply adsorbed TiO_2-supported copper.

For the adsorption of 4 hydrogen atoms (shown in **Figures 7 (c)** and **(d)),** the average computed hydrogen adsorption free energy, ΔG_H ranges from -0.25 to -0.76 eV. For adsorption of 5 hydrogen atoms (**Figures 7 (e)** and **(f)**) ΔG_H ranges from -0.19 to -0.30

eV. These results suggest that hydrogen adsorption is too strong at at Cu-modified TiO_2, when considering the energy per adsorbed H atom. This would not be consistent with the experimental findings.

By contrast, if we computed $\Delta\Delta G_H$ for 4 H atoms, relative to 3 adsorbed H atoms, then the free energy of adsorption on Cu/TiO_2 is 0 and -0.18 eV. Similarly for five adsorbed H atoms, we found two hydrogen adsorption configurations, shown in **Figures 7 (e)** and **(f)**, where the adsorption energies computed in this manner are -0.07 and -0.05 eV. Thus, the addition of hydrogen atoms to these coverages result in adsorption free energies which are well within the target range of computed adsorption free energies. We see that the H adsorption configuration in **Figure 7 (f)** shows spontaneous formation of a H_2 molecule upon relaxation so that at this coverage, the adsorption free energies are favourable towards HER.

On the Pd/TiO_2 heterostructure, for which the H adsorption structures are shown in **Figure 8** the computed ΔG_H for 2 H atoms (**Figure 8 (a)**) is -0.13 eV; other adsorption modes have average adsorption energies of -0.35 – - 0.45 eV, which would suggest that H atoms at this coverage can be too strongly bound to the supported Pd rod. Using $\Delta\Delta G_H$, the computed adsorption energy with the first H atom already adsorbed is -0.30 eV, similar to pure copper so that at this coverage of hydrogen adsorption of the H atoms at supported Pd is too strong.

If we compute $\Delta\Delta G_H$ for 4 adsorbed atoms, starting from 3 adsorbed H atoms on Pd/TiO_2, the computed adsorption free energy is -0.07 eV. For 5 H atoms, the configuration shown in **Figure 8 (c)** has a computed adsorption free energy of 0.01 eV suggesting that at higher H coverages the Pd-modified TiO_2 will promote HER when the surface of the metal already has H atoms adsorbed, similar to pure copper.

On the single Pd-doped Cu/TiO_2 structure, the computed ΔG_H for two H atoms is -0.19 eV per H atom, outside the range of relevant H adsorption energies, while other adsorption sites have average adsorption free energies of -0.3 to -0.4 eV. The preference is for H adsorption at both copper and Pd sites, **Figure 9**. The computed $\Delta\Delta G_H$ is -0.04 eV, which is very close to the ideal 0 eV value and suggests that for low H coverage, adsorption of hydrogen at the localised Pd site, so that both Cu-H and Pd-H bonds are present, can promote the HER in this dilute bimetallic system. For the adsorption of 4 hydrogen atoms, the computed $\Delta\Delta G_H$ is -0.05 and -0.07 eV relative to three H atoms, so this composition promotes the HER and the for adsorption of 5 H the computed $\Delta\Delta G_H$ is -0.02 eV. Thus, up to 5 H atoms can be easily accommodated with a low Pd content in this structure and high activity to HER is shown.

Finally, considering the core shell Cu@Pd/TiO_2 structure, for which the H adsorption structures are shown in **Figure 10**, the computed ΔG_H for two adsorbed H atoms is -0.81 and -0.78 eV per H atom which suggests far too strong adsorption of hydrogen at the Pd shell at this hydrogen coverage. However, if we use $\Delta\Delta G_H$ then the computed free energies for these configurations are +0.02 and +0.09 eV which are close to the ideal value of ΔG_H.

The binding of H in both structures is exclusively to Pd atoms, but is also more favourable than for the pure Pd/TiO_2 structure. This suggests that the Cu core plays a role in moderating the adsorption of H atoms at the Pd at low H coverages. Based on the Bader charge analysis, the presence of reduced Pd sites in Cu@Pd/TiO_2 systems appears to be important for promoting H adsorption. By contrast, the typical metallic Pd sites in the pure Pd structure do not particularly promote H adsorption. The computed $\Delta\Delta G_H$ for 4 H atoms is -0.28 eV which is outside the target energy range, and for 5 H atoms $\Delta\Delta G_H$ is -0.19 and -0.2 eV. Thus, the optimum H coverage with adsorption free energies that

promote HER appears to be sensitive to the composition of the supported Cu@Pd bimetallic structure.

These DFT results show that the incorporation of Pd into supported Cu structures can help promote the HER and that the coverage of hydrogen at the supported metal also plays an important role, as previously discussed for HER on metal phosphides and nitrides.[71,72] Indeed, it has been found that for PtCu co-catalyst on TiO_2 it has been observed a synergistic activity enhancement and a significantly higher activity toward photocatalytic H_2 evolution with respect to the monometallic Pt- or Cu/TiO_2 catalysts.[73] These authors proposed that the enhanced activity could be due to Pt–Cu electronic interactions, where Cu increases the electron density on Pt, favoring a more efficient electron transfer for H_2 evolution. We note that a small amount of Pd incorporated into Cu promotes H adsorption at all coverages examined, while the Cu-core-Pd-shell structure with a significantly higher Pd content promotes HER at the moderate hydrogen coverages and is less favourable at the lowest and highest H coverages. Similarly, the pure Pd system appears to be more effective for promoting HER at high hydrogen coverages, while Cu is particularly effective at low H coverages. One origin for this is that as H is adsorbed at the Pd-rich structures, Pd atoms neighbouring the adsorption site become partially reduced and this provides higher energy electronic states that can interact with H states and prevent overstabilisation of H atom adsorption.

CONCLUSIONS

By a simple deposition method, we have controlled the incorporation of increasing amount of palladium onto Cu/TiO_2 system. Thus, by redox displacement it is possible to substitute Pd by Cu which has been previously photodeposited into TiO_2 support. This controlled sequential deposition guarantees the dispersion and a strong interaction

between Cu and Pd. Moreover, the obtained bimetallic clusters showed a small size with a narrow distribution with a Cu@Pd core-shell structure.

DFT results on models of Cu@Pd bimetallic 1D rod supported on rutile TiO_2 show that the preference is for Pd to incorporate in the shell of the structure forming a Cu core-Pd shell structure. Investigation of the adsorption free energy of hydrogen studies clearly point out that the incorporation of Pd into supported Cu structures can help promote the HER and that the coverage of hydrogen at the supported metal also plays an important role.

This way, the H_2 production by isopropanol photoreforming reaction is strongly affected by the incorporation of even very low amounts of palladium. At long-term reaction times, the efficiencies obtained for $Cu@Pd_{0.5}$ system is notably enhanced with respect to former Cu and Pd monometallic references. The formation of a core-shell structure would stabilize both metals against deactivation at longer reaction times. This result would demonstrate that the formation of a bimetallic core-shell nanostructuration, would be a promising strategy for developing more stable and highly active systems for H_2 production.

ACKNOWLEDGMENTS

GC acknowledges the financial support by PCIN-2017-056 project from M-ERA.Net programme through Acciones Programación Conjunta (Ministerio de Ciencia e Innovación). MN acknowledges support from Science Foundation Ireland through the Horizon 2020 M-ERA.net cofund program, project RATOCAT, grant numbers 685451 and SFI 17/M-ERA/3418 and access to computational resources at Tyndall and through the Irish Center for High End Computing (ICHEC), www.ichec.ie.

ASSOCIATED CONTENT.

Supporting Information

Tables from different characterization analysis. Additional Figures: Flow reaction scheme, evolution of Cu and Pd loading measured from ICP analysis, structural and surface characterization, TEM analysis of fresh and used Cu@Pd samples, diffuse reflectance UV-vis spectra.

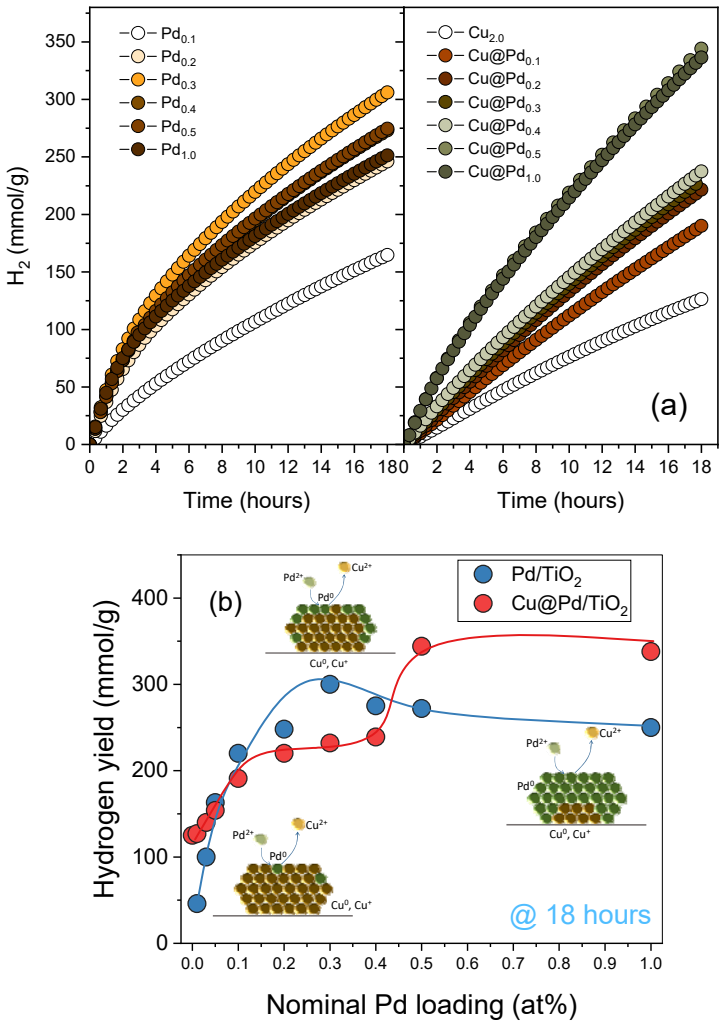


Figure 1. Photocatalytic activity for isopropanol photoreforming: a) H_2 production evolution with time for mono- and bimetallic Cu@Pd doped TiO_2 systems 18 hours of reaction; b) H_2 production after 18 hours of reaction for mono- and bimetallic Cu@Pd doped TiO_2 systems.

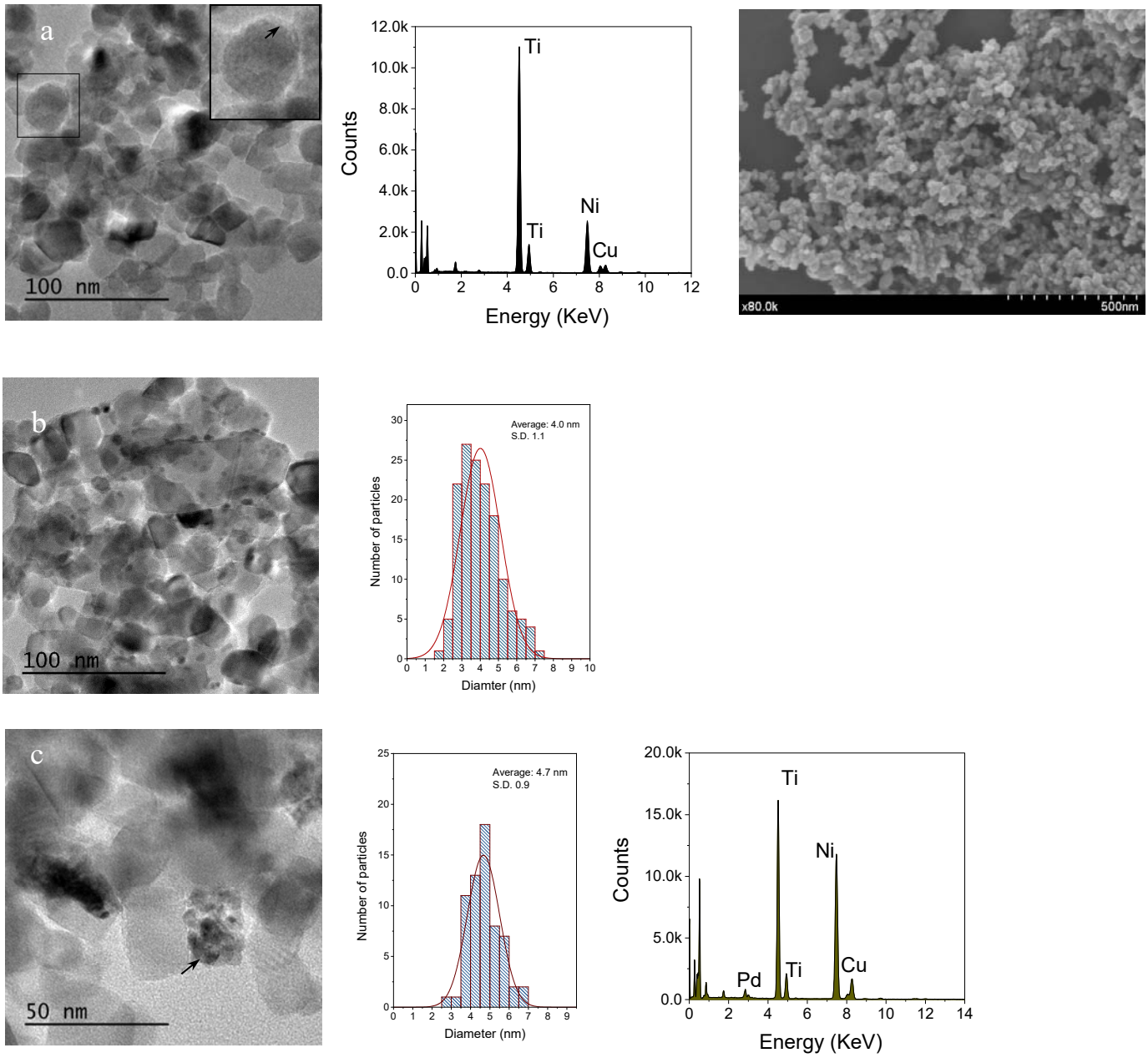


Figure 2. TEM/SEM analysis for: a) $Cu_{2.0}/TiO_2$; b) $Pd_{1.0}/TiO_2$; and c) $Cu@Pd_{1.0}/TiO_2$ samples.

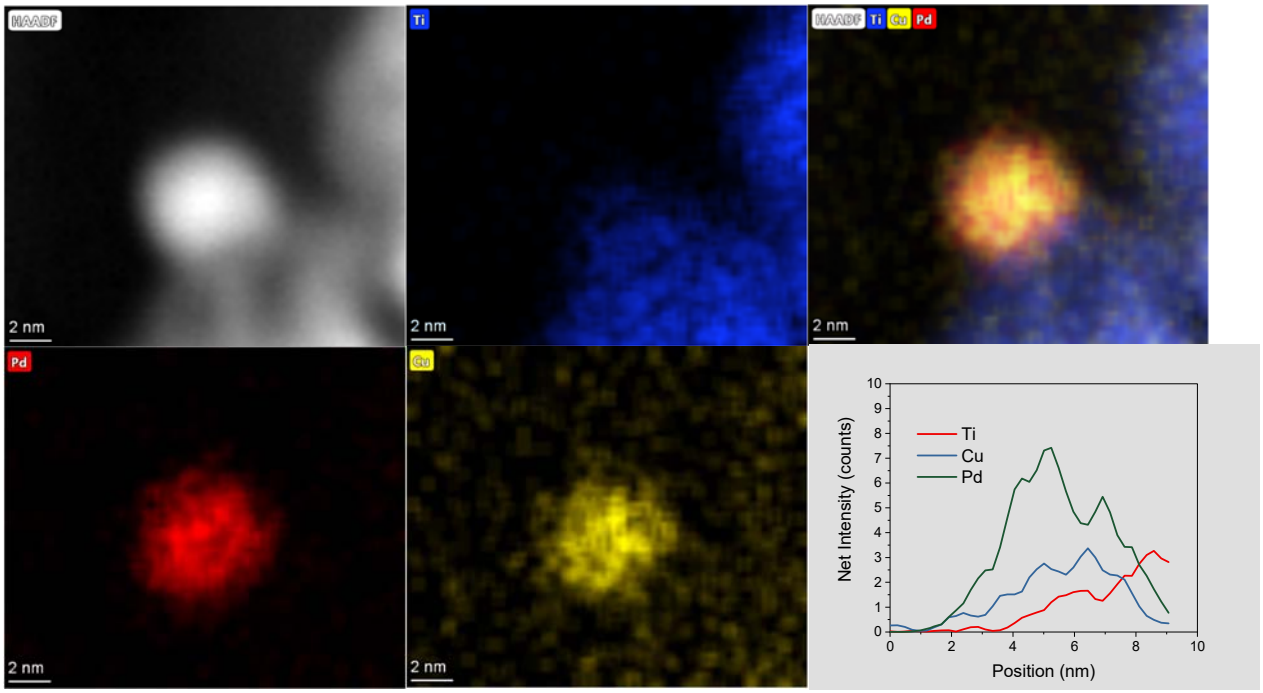


Figure 3. HAADF−STEM image and EDX maps of Pd, Cu and Ti for Cu@$Pd_{0.3}/TiO_2$ sample.

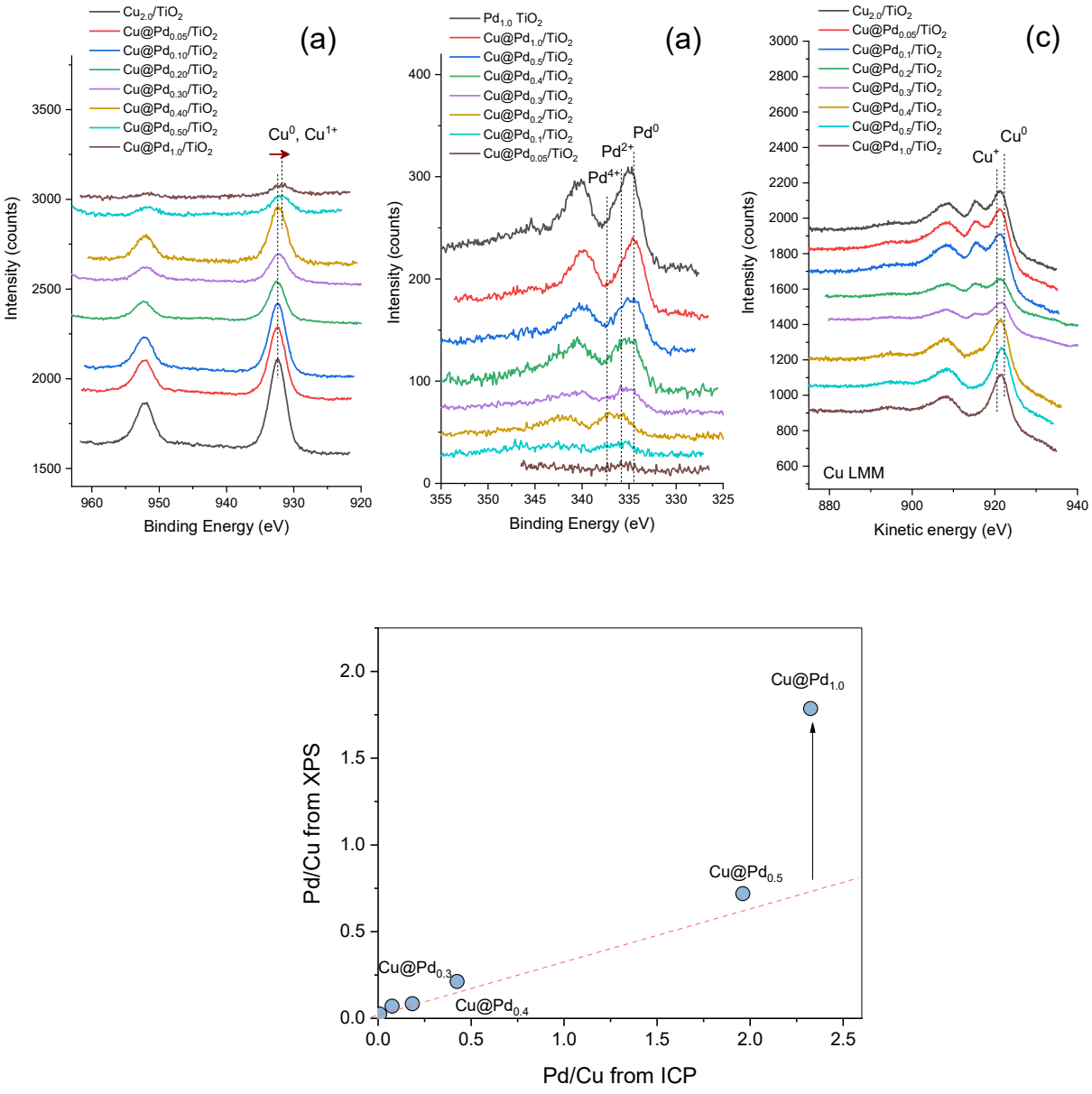


Figure 4. Upper row: XPS analysis: a) Cu *2p* spectra; b) Pd *3d* spectra; c) Cu *LMM* Auger spectra for different Cu@Pd/TiO_2 systems. Lower row: Evolution of Pd/Cu ratio from XPS with respect to Pd/Cu ratio obtained from ICP analysis.

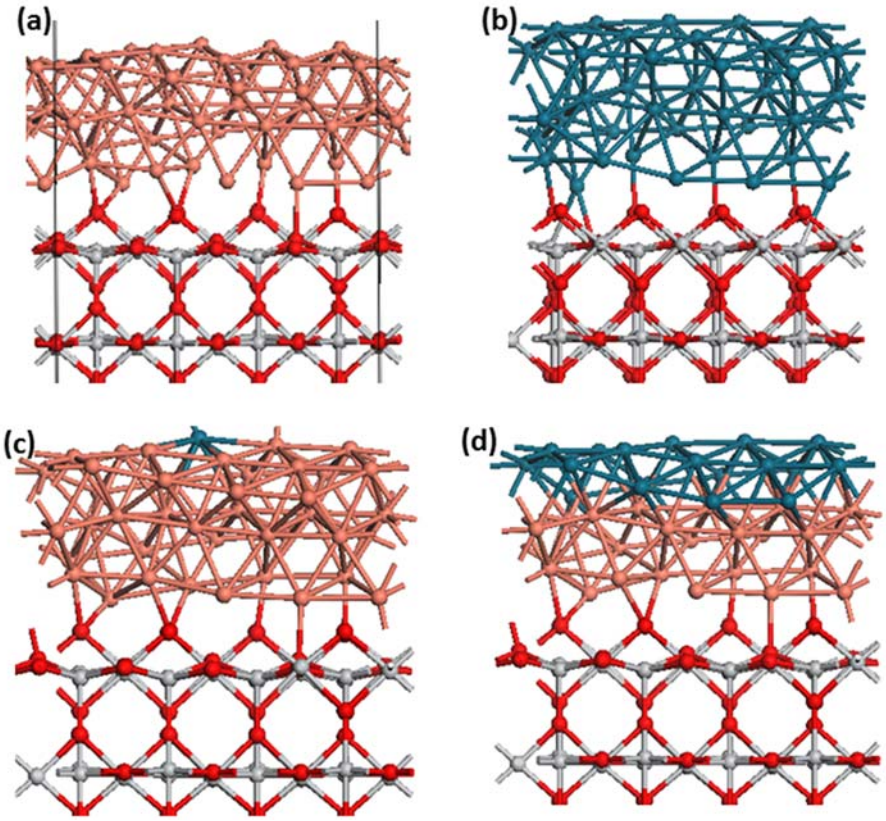


Figure 5. Atomic structure of rutile TiO_2 (110) modified with **(a):** Cu_{42}, **(b):** Pd_{42}, **(c):** $Cu_{41}Pd$ and **(d)** core-shell $Cu_{24}Pd_{18}$. *Colour coding*: Ti – grey spheres, O – red spheres, Cu – brown spheres and Pd – blue spheres.

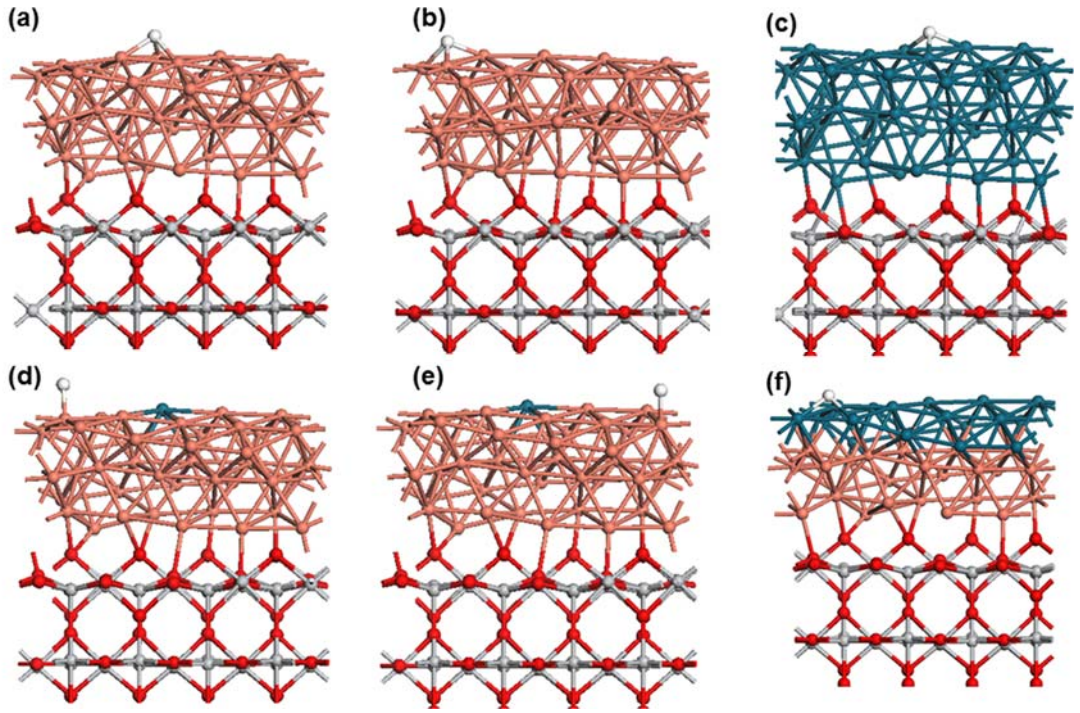


Figure 6. Atomic structures for those adsorption structures for adsorbed 1 hydrogen atom with free energies between -0.15 and 0.15 eV, referenced to half the total energy of a free H_2 molecule. **(a), (b)** Cu/TiO_2, **(c)** Pd/TiO_2, **(d)**, **(e)** $1PdCu/TiO_2$ and **(f)** core-shell $Cu@Pd/TiO_2$. Colour coding is the same as **Figure 5**, with the addition of white spheres for hydrogen atoms.

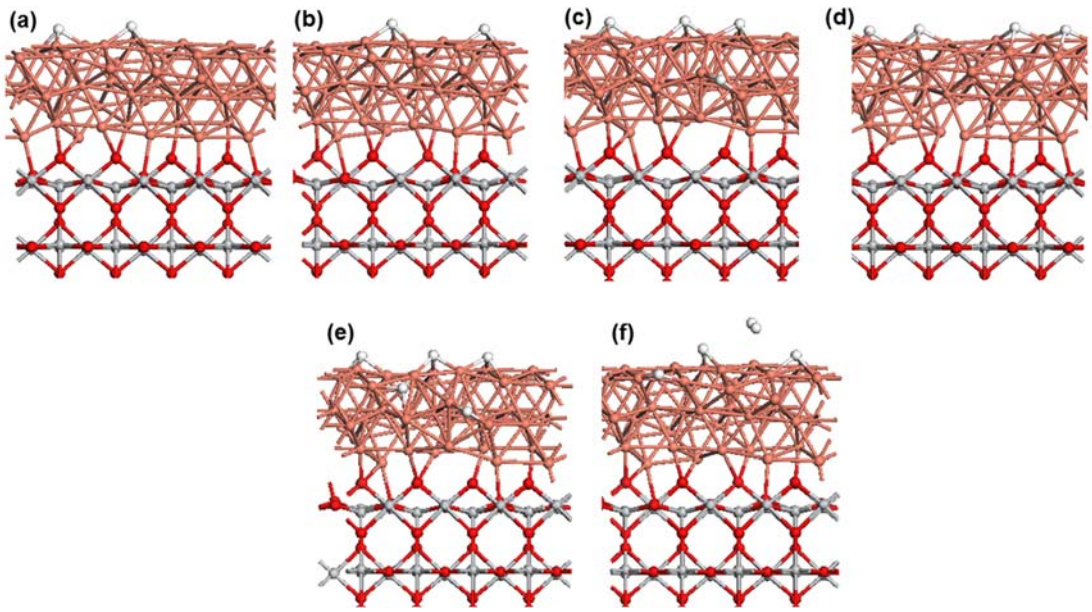


Figure 7. Atomic structures for H adsorption on Cu/TiO_2. **(a), (b)** 2 adsorbed hydrogen atoms, **(c)**, **(d)** 4 H **(e), (f)** 5 H. Colour coding is the same as **Figure 6**.

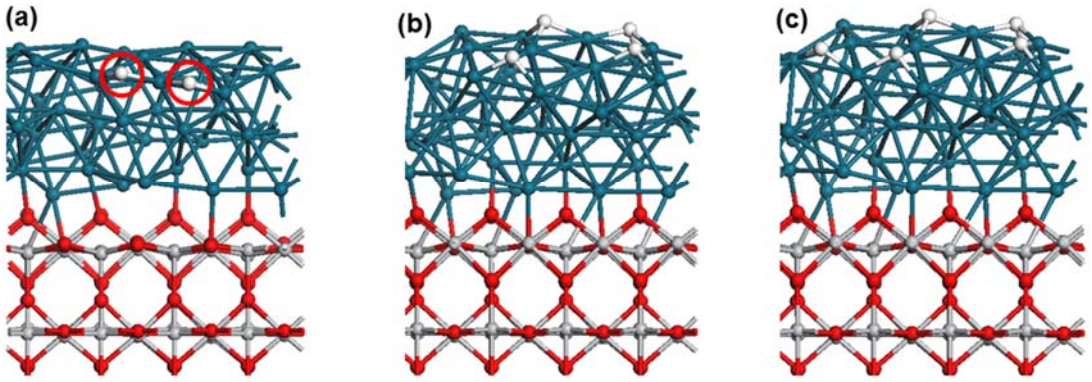


Figure 8. Atomic structures for H adsorption on Pd/TiO_2. **(a)** 2 adsorbed hydrogen atoms, **(b)**, 4 adsorbed H atoms **(c)** 5 adsorbed H atoms. Colour coding is the same as **Figure 6**.

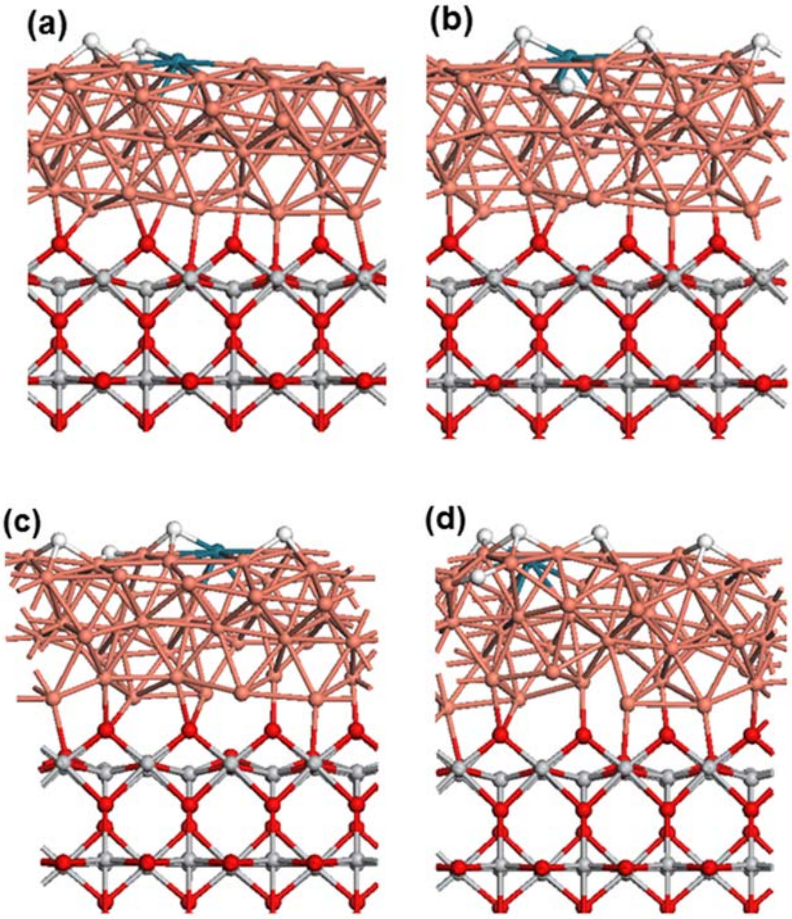


Figure 9. Atomic structures for H adsorption on 1PdCu/TiO_2. **(a)** 2 adsorbed hydrogen atoms, **(b), (c)**, 4 adsorbed H **(d)** 5 adsorbed H. Colour coding is the same as **Figure 6**.

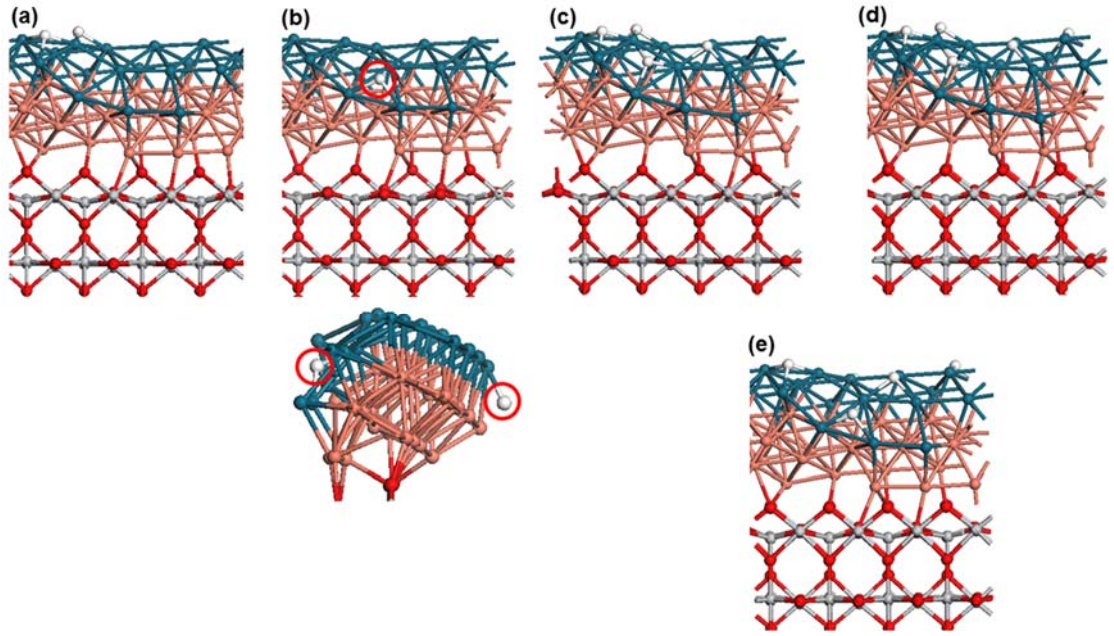


Figure 10. Atomic structures for H adsorption on core-shell Cu@Pd/TiO_2. **(a), (b)** 2 adsorbed hydrogen atoms, **(c)** 4 adsorbed H **(d), (e)** 5 adsorbed H. Under part **(b)** we show a side view so the two H adsorption sites are visible, indicated by the red rings. Colour coding is the same as **Figure 6**.

REFERENCES

1. Christoforidis, K.C.; Fornasiero, P. Photocatalytic Hydrogen Production: A Rift into the Future Energy Supply. *ChemCatChem* **2017**, *9*, 1523 –1544.

2. Kubacka, A.; Fernández-García, M.; Colón, G. Advanced Nanoarchitectures for Solar Photocatalytic Applications. *Chem. Rev.* **2012**, *112*, 1555–1614.

3. Maldonado, M.I.; López-Martín, A.; Colón, G.; Peral, J; Martínez-Costa, J.I.; Malato, S. Solar Pilot Plant Scale Hydrogen Generation by Irradiation of Cu/TiO_2 Composites in Presence of Sacrificial Electron Donors. *Appl. Catal. B: Environ.* **2018**, *229*, 15–23.

4. Colón, G. Towards the Hydrogen Production by Photocatalysis. Appl. Catal. A: Gen. **2016**, 518, 48–59

5. Naldoni, A.; D'Arienzo, M.; Altomare, M.; Marelli, M. Scotti, R.; Morazzoni, F.; Selli, E.; Dal Santo, V. Pt and Au/TiO_2 Photocatalysts for Methanol Reforming: Role of Metal Nanoparticles in Tuning Charge Trapping Properties and Photoefficiency. *Appl. Catal. B: Environ.*, **2013**, *130-131*, 239–248.

6. Puga, A.V.; Forneli, V.; García, H.; Corma, A. Production of H_2 by Ethanol Photoreforming on Au/TiO_2. *Adv. Funct. Mater.* **2014**, *24*, 241–248.

7. Su, R.; Tiruvalam, R.; Logsdail, A.J.; He, Q.; Downing, C.A.; Jensen, M.T.; Dimitratos, N.; Kesavan, L.; Wells, P.P.; Bechstein, R.; Jensen, H.H.; Wendt, S.; Catlow, C.R.A.**;** Kiely, C.J.; Hutchings, G.J. ; Besenbacher, F. Designer Titania-Supported Au–Pd Nanoparticles for Efficient Photocatalytic Hydrogen Production. ACS *Nano*, **2014**, *8*, 3490–3497.

8. Mei, B.; Han, K.; Mul, G. Driving Surface Redox Reactions in Heterogeneous Photocatalysis: The Active State of Illuminated Semiconductor-Supported Nanoparticles during Overall Water-Splitting. *ACS Catal.* **2018**, *8*, 9154–9164.

9. Park, S.Y.; Han, K.; O'Neill, D.B.; Mul, G. Stability of Ag@SiO_2 Core–Shell Particles in Conditions of Photocatalytic Overall Water-Splitting. *J. Energy Chem.* **2017**, *26*, 309–314.

10. Melvin, A.A.; IIIath, K.; Das, T.; Raja, T.; Bhattacharyya, S.; Gopinath, C.S. M–Au/TiO_2 (M = Ag, Pd, and Pt) Nanophotocatalyst for Overall Solar Water Splitting: Role of Interfaces. *Nanoscale*, **2015**, *7*, 13477–13488.

11. Y. Liu, X. Gu, W. Qi, H. Zhu, H. Shan, W. Chen, P. Tao, C. Song, W. Shang, T. Deng, J. Wu, Enhancing the Photocatalytic Hydrogen Evolution Performance of a Metal/Semiconductor Catalyst through Modulation of the Schottky Barrier Height by Controlling the Orientation of the Interface. *ACS Appl. Mater. Interfaces*, **2017**, *9*, 12494–12500.

12. Ampelli, C.; Passalacqua, R.; Genovese, C.; Perathoner, S.; Centi, G.; Montini, T.; Gombac, V.; Delgado Jaen, J.J.; Fornasiero, P. H_2 Production by Selective Photo-Dehydrogenation of Ethanol in Gas and Liquid Phase on CuO_x/TiO_2 Nanocomposites. *RSC Adv.*, **2013**, *3*, 21776–21788.

13. Valero, J.M.; Obregón, S.; Colón, G. Active Site Considerations on the Photocatalytic H_2 Evolution Performance of Cu-Doped TiO_2 Obtained by Different Doping Methods. *ACS Catal.* **2014**, *4*, 3320−3329.

14. Muñoz-Batista, M.J.; Motta Meira, D.; Colón, G.; Kubacka, A.; Fernández-García, M. Phase-Contact Engineering in Mono- and Bimetallic Cu-Ni Co-catalysts for Hydrogen Photocatalytic Materials. *Angew. Chem. Int. Ed.* **2018**, *57*, 1199 –1203.

15. Caudillo-Flores, U.; Muñoz-Batista, M.J.; Fernández-García, M.; Kubacka, A. Bimetallic Pt-Pd Co-Catalyst Nb-doped TiO_2 Materials for H_2 Photo-Production under UV and Visible Light Illumination. *Appl. Catal. B: Environ.*, **2018**, *238*, 533–545.

16. Kavitha, R.; Kumar, S.G. Review on bimetallic-deposited TiO_2: preparation methods, charge carrier transfer pathways and photocatalytic applications. *Chem. Pap.* **2020**, *74,* 717–756.

17. Murcia-López, S.; González-Castaño, M.; Flox, C.; Morante, J.R.; Andreu, T. On the Role of Cu, Ag and Pt in Active Titania for Gas-Phase Ethanol Photo-Reforming. *Mater. Sci. Semicond. Process.* **2018**, *73*, 30–34.

18. Luna, A.L.; Dragoe, D.; Wang, K.; Beaunier, P.; Kowalska, E.; Ohtani, B.; Bahena Uribe, D.; Valenzuela, M.A.; Remita, H.; Colbeau-Justin, C. Photocatalytic Hydrogen Evolution Using Ni–Pd/TiO_2: Correlation of Light Absorption, Charge-Carrier Dynamics, and Quantum Efficiency. *J. Phys. Chem. C* **2017**, *121*, 14302–14311.

19. Luna, A.L.; Novoseltceva, E.; Louarn, E.; Beaunier, P.; Kowalska, E.; Ohtani, B.; Valenzuela, M.A.; Remita, H.; Colbeau-Justin, C. Synergetic Effect of Ni and Au Nanoparticles Synthesized on Titania Particles for Efficient Photocatalytic Hydrogen Production. *Appl. Catal. B: Environ.* **2016**, *191*, 18–28.

20. Miyazaki, M.; Furukawa, S.; Takayama, T.; Yamazoe, S.; Komatsu, T. Surface Modification of PdZn Nanoparticles via Galvanic Replacement for the Selective Hydrogenation of Terminal Alkynes. *ACS Appl. Nano Mater.* **2019**, *2*, 5, 3307–3314.

21. Furthmüller, J.; Hafner, J.; Kresse, G. Dimer Reconstruction and Electronic Surface States on Clean and Hydrogenated Diamond (100) Surfaces. *Phys. Rev. B.*, **1996**, *53*, 7334-7351.

22. Kresse, G.; Joubert, D. From Ultrasoft Pseudopotentials to the Projector Augmented-Wave Method. *Phys. Rev. B*., **1999**, *59*, 1758-1775.

23. Perdew, J.P.; Chevary, J.A.; Vosko, S.H.; Jackson, K.A.; Pederson, M.R.; Singh, D.J.; Fiolhais, C. Atoms, Molecules, Solids, and Surfaces: Applications of the Generalized Gradient Approximation for Exchange and Correlation. *Phys. Rev. B* **1992**, *46*, 6671-6687.

24. Anisimov, V.I.; Zaanen, J.; Andersen, O.K. Band Theory and Mott Insulators: Hubbard U Instead of Stoner I. *Phys. Rev. B.*, **1991**, *44*, 943-954.

25. Fronzi, M.; Iwaszuk, A.; Lucid, A.; Nolan, M. Metal Oxide Nanocluster-Modified TiO_2 as Solar Activated Photocatalyst Materials. *J. Phys. Condens. Matter*, **2016**, *28*, 074006.

26. Fronzi, M.; Nolan, M. Surface Modification of Perfect and Hydroxylated TiO_2 Rutile (110) and Anatase (101) with Chromium Oxide Nanoclusters. *ACS Omega*, **2017**, *2*, 6795-6808.

27. Morgan, B.J.; Watson, G.W. A DFT+U Description of Oxygen Vacancies at the TiO_2 Rutile (110) Surface. *Surf. Sci.*, **2007**, *601*, 5034-5041.

28. Haselmann, G.M.; Eder, D. Early-Stage Deactivation of Platinum-Loaded TiO_2 Using In Situ Photodeposition during Photocatalytic Hydrogen Evolution. *ACS Catal.* **2017**, *7*, 4668-4675.

29. van Deelen, T.W.; Hernández Mejía, C.; de Jong, K.P. Control of Metal-Support Interactions in Heterogeneous Catalysts to Enhance Activity and Selectivity. *Nat. Catal.* **2019**, *2*, 955–970.

30. Fujiwara, K; Okuyama, K.; Pratsinis. S.E. Metal–Support Interactions in Catalysts for Environmental Remediation. Environ. Sci.: *Nano*, **2017**, *4*, 2076-2092.

31. Zhang, N.; Xu, Y.J. Aggregation- and Leaching-Resistant, Reusable, and Multifunctional Pd@CeO_2 as a Robust Nanocatalyst Achieved by a Hollow Core–Shell Strategy. *Chem. Mater.* **2013**, *25*, 9, 1979–1988.

32. Mu, Y.; Zhang, H.; Zheng, W.; Cui, X. Highly stable Au/Pd@mesoporous SiO_2 yolk–shell hetero-nanostructures for plasmon-enhanced visible light driven catalytic reactions. *New J. Chem.*, **2017**, *41*, 786-792.
33. Husin, H.; Su, W.N.; Pan, C.J.; Liu, J.Y.; Rick, J.; Yang, S.C.; Chuang, W.T.; Sheu, H.S.; Hwang, B.J. Pd/NiO Core/Shell Nanoparticles on $La_{0.02}Na_{0.98}TaO_3$ Catalyst for Hydrogen Evolution from Water and Aqueous Methanol Solution. *Int. J. Hydrogen Energ.* **2013**, *38*, 13529-13540.
34. Toe, C.Y.; Zheng, Z.; Wu, H.; Scott, J.; Amal, R.; Ng, Y.H. Photocorrosion of Cuprous Oxide in Hydrogen Production: Rationalising Self-Oxidation or Self-Reduction. *Angew. Chem. Int. Ed.*, **2018**, 57, 13613–13617.
35. Velazquez, J.J.; Fernández-González, R.; Díaz, L.; Pulido Melian, E.; Rodríguez, V.D.; Núñez, P. Effect of Reaction Temperature and Sacrificial Agent on the Photocatalytic H_2-Production of Pt-TiO_2. *J. Alloys Compd.* **2017**, *721*, 405-410.
36. Al-Azri, Z.H.H.; Chen, W.T.; Chan, A.; Jovic, V.; Ina, T.; Idriss, H.; Waterhouse, G.I.N. The Roles of Metal Co-Catalysts and Reaction Media in Photocatalytic Hydrogen Production: Performance Evaluation of M/TiO_2 Photocatalysts [M = Pd, Pt, Au] in Different Alcohol–water Mixtures. *J. Catal.* **2015**, *329*, 355-367.
37. Spanu, D.; Minguzzi, A.; Recchia, S.; Shahvardanfard, F.; Tomanec, O.; Zboril, R.; Schmuki, P.; Ghigna, P.; Altomare, M. An Operando X-ray Absorption Spectroscopy Study of a NiCu−TiO_2 Photocatalyst for H_2 Evolution. *ACS Catal.* **2020**, *10*, 15, 8293–8302.
38. Colón, G.; Maicu, M.; Hidalgo, M.C.; Navío, J.A. Cu-Doped TiO_2 Systems with Improved Photocatalytic Activity. *Appl. Catal. B: Environ.* **2006**, *67*, 41–51.
39. Hou , T.; Luo, N.; Li, H.; Heggen, M.; Lu, J.; Wang, Y.; Wang, F.Yin and Yang Dual Characters of CuOx Clusters for C–C Bond Oxidation Driven by Visible Light. *ACS Catal.* **2017**, *7*, 3850–3859.
40. Wang, D.; Pan, X.; Wang, G.; Yi, Z. Improved Propane Photooxidation Activities Upon Nano Cu_2O/TiO_2 Heterojunction Semiconductors at Room Temperature. *RSC Adv.*, **2015**, *5*, 22038–22043
41. Clarizia, L.; Vitiello, G.; Luciani, G.; Di Somma, I.; Andreozzi, R.; Marotta, R. *In Situ* Photodeposited NanoCu on TiO_2 as a Catalyst for Hydrogen Production Under UV/Visible Radiation. *Appl. Catal. A: Gen.* **2016**, *518*, 142–149.
42. Li, Y.F.; Dong, F.X.; Chen, Y.; Zhang, X.L.; Wang, L.; Bi, Y.G.; Tian, Z.N.; Liu, Y.F.; Feng, J.; Sun, H.B. As-Grown Graphene/Copper Nanoparticles Hybrid Nanostructures for Enhanced Intensity and Stability of Surface Plasmon Resonance. *Sci. Reports* **2016**, *6*, 37190.
43. Huang, S. ; Yu, Y.; Yan, Y.; Yuan, J.; Yin, S.; Cao, Y. Enhanced Photocatalytic Activity of TiO_2 Activated by Doping Zr and Modifying Pd. *RSC Adv.*, **2016**, *6*, 29950–29957.
44. Mishra, A.; Mehta, A.; Kainth, S.; Basu, S. Effect of Different Plasmonic Metals on Photocatalytic Degradation of Volatile Organic Compounds (VOCs) by Bentonite/M-TiO_2 Nanocomposites under UV/visible Light. *Appl. Clay Sci.* **2018**, *153*, 144–153
45. Morán-Pineda, M.; Castillo, S.; Asomoza, M.; Gómez, R. Copper Oxide on Cu/Al_2O_3-TiO_2 Catalysts TG, FTIR-CO Absorption and Catalytic Activity in the NO Reduction by CO. *J. Thermal Analysis and Calorimetry*, **2003**, *73*, 341–346.
46. Coloma, F.; Márquez, F.; Rochester, C.H.; Anderson, J.A. Determination of the Nature and Reactivity of Copper Sites in Cu–TiO_2 Catalysts. *Phys. Chem. Chem. Phys.* **2000**, *2*, 5320–5327.
47. McCue, A.C.; McRitchie, C.J.; Shepherd, A.M.; Anderson, J.A. Cu/Al_2O_3 Catalysts Modified with Pd for Selective Acetylene Hydrogenation. *J. Catal.* **2014**, *319*, 127–135.

48. Schumann, J.; Kröhnert, J.; Frei, E.; Schlögl, R.; Trunschke, A. IR-Spectroscopic Study on the Interface of Cu-Based Methanol Synthesis Catalysts: Evidence for the Formation of a ZnO Overlayer. *Top. Catal.* **2017**, 60, 1735–1743.

49. Spezzati, G.; Su, Y.; Hofmann, J.P.; Benavidez, A.D.; De La Riva, A.T.; McCabe, J.; Datye, A.K.; Hensen, E.J.M. Atomically Dispersed Pd–O Species on CeO_2(111) as Highly Active Sites for Low-Temperature CO Oxidation. *ACS Catal.* **2017**, *7*, 6887–6891.

50. Ström, L.; Ström, H.; Carlsson, P.A.; Skoglundh, M.; Härelind, H. Catalytically Active Pd–Ag Alloy Nanoparticles Synthesized in Microemulsion Template. *Langmuir* **2018**, *34*, 9754–9761.

51. Chen, P.; Khetan, A.; Yang, F.; Migunov, V.; Weide, P.; Stürmer, S.P.; Guo, P.; Kähler, K.; Xia, W.; Mayer, J.; Pitsch, H.; Simon, U.; Muhler, M. Experimental and Theoretical Understanding of Nitrogen-Doping-Induced Strong Metal–Support Interactions in Pd/TiO_2 Catalysts for Nitrobenzene Hydrogenation. *ACS Catal.* **2017**, *7*, 1197–1206.

52. Maimaiti, Y.; Nolan, M.; Elliott, S.D. Reduction Mechanisms of the CuO(111) Surface Through Surface Oxygen Vacancy Formation and Hydrogen Adsorption. *Phys. Chem. Chem. Phys.* 2014, *16*, 3036-3046.

53. Kim, Y.; Kim, J.; Kim, D.H. Investigation on the Enhanced Catalytic Activity of a Ni-Promoted Pd/C Catalyst for Formic Acid Dehydrogenation: Effects of Preparation Methods and Ni/Pd Ratios. *RSC Adv.* **2018**, *8*, 2441–2448.

54. Zhu, Y.; Liu, D.; Meng, M. H_2 Spillover Enhanced Hydrogenation Capability of TiO_2 Used for Photocatalytic Splitting of Water: A Traditional Phenomenon for New Applications. *Chem. Comm.* **2014**, *50*, 6049–6051

55. Noronha, F.B.; Schmal, M.; Primet, M.; Frety, R. Characterization of Palladium-Copper Bimetallic Catalysts Supported on Silica and Niobia. *Appl. Catal.* **1991**, *78*, 125–139.

56. Batista, J.; Pintar, A.; Mandrino, D.; Jenko, M.; Martin, V. XPS and TPR Examinations of γ-Alumina-Supported Pd-Cu catalysts. *Appl. Catal. A: Gen.* **2001**, *206*, 113–124.

57. Espinós, J.P.; Morales, J.; Barranco, A.; Caballero, A.; Holgado, J.P.; González-Elipe, A.R. Interface Effects for Cu, CuO, and Cu_2O Deposited on SiO_2 and ZrO_2. XPS Determination of the Valence State of Copper in Cu/SiO_2 and Cu/ZrO_2 Catalysts. *J. Phys. Chem. B*, **2002**, *106*, 6921–6929.

58. Ye, S.H.; Feng, J.X.; Li, G.R. Pd Nanoparticle/CoP Nanosheet Hybrids: Highly Electroactive and Durable Catalysts for Ethanol Electrooxidation. *ACS Catal.* **2016**, *6*, 7962–7969.

59. Ji, Y.; Ying, Y.; Pan, Y.; Li, M.; Guo, X.; Wu, Y.; Wen, Y.; Yang, H. Palladium Networks Decorated by Cuprous Oxide for Remarkably Enhanced Electrocatalytic Activity of Methanol Oxidation Reaction with High CO-Tolerance. *J. Power Sources*, **2016**, *329*, 115–122.

60. Koga, H.; Tada, K.; Okumura, M. DFT Study of CO Oxidation over Au/TiO_2(1 1 0): The Extent of the Reactive Perimeter Zone. *Chem. Phys. Lett.* **2014**, *610*, 76-81

61. Koga, H.; Tada, K.; Okumura, M. Density Functional Theory Study of Active Oxygen at the Perimeter of Au/TiO_2 Catalysts. *J. Phys. Chem. C* **2015**, *119*, 25907- 25916

62. Strayer, M.E.; Senftle, T.P.; Winterstein, J.P.; Vargas-Barbosa, N.M.; Sharma, R.; Rioux, R.M.; Janik, M.J. Mallouk; T.E. Charge Transfer Stabilization of Late Transition Metal Oxide Nanoparticles on a Layered Niobate Support. *J. Am. Chem. Soc.* **2015**, *137*, 16216–16224.

63. Chen, L.J.; Tang, Y.; Cui, L.; Ouyang, C.; Shi, S. Charge Transfer and Formation of Ce^{3+} upon Adsorption of Metal Atom M (M = Cu, Ag, Au) on CeO_2 (100) Surface. *J. Power Sources* **2013**, *234*, 69-81.

64. Zhu, K.J.; Liu, J.; Yang, Y.J.; Xu, Y.X.; Teng, B.T.; Wen, X.D.; Fan, M. A Method to Explore the Quantitative Interactions Between Metal and Ceria for M/CeO_2 Catalysts. *Surf. Sci.*, **2018**, *669*, 79-86.

65. Maimaiti, Y.; Nolan, M.; Elliott, S.D. *Phys. Chem. Chem. Phys.* **2014**, *16*, 3036-3046.

66. Sharma, P.K.; Cortes, M.A.L.R.M.; Hamilton, J.W.J.; Han, Y.; Byrne, J.A.; Nolan, M. *Catalysis Today* **2019**, *321*, 9–17.

67. Jäger, M.O.J.; Morooka, E.V.; Federici Canova, F.; Himanen, L.; Foster, A.S. Machine Learning Hydrogen Adsorption on Nanoclusters Through Structural Descriptors, *npj Computational Materials*, **2018**, *4*, 37.

68. Hu, G.; Tang, Q.; Jiang, D.E. CoP for Hydrogen Evolution: Implications from Hydrogen Adsorption. *Phys. Chem. Chem. Phys.*, **2016**, *18*, 23864–23871.

69. Bonde, J.; Moses, P.G.; Jaramillo, T.F.; Nørskov, J.K.; Chorkendorff, I. Hydrogen Evolution on Nano-Particulate Transition Metal Sulphides. *Faraday Discuss.* **2009**, *140*, 219–231.

70. Tsai, C.; Chan, K.; Abild-Pedersen, F.; Nørskov, J.K. Active Edge Sites in $MoSe_2$ and WSe_2 Catalysts for the Hydrogen Evolution Reaction: A Density Functional Study. *Phys. Chem. Chem. Phys.*, **2014**, *16*, 13156-13164.

71. Abghoui, Y.; Skúlason, E. Hydrogen Evolution Reaction Catalyzed by Transition-Metal Nitrides. *J. Phys. Chem. C* **2017**, *121*, 24036–24045.

72. Partanen, L.; Hakala, M.; Laasonen, K. Hydrogen Adsorption Trends on Various Metal-Doped Ni_2P Surfaces for Optimal Catalyst Design. *Phys. Chem. Chem. Phys.*, **2019**, *21*, 184–191.

73. Shahvaranfard, F.; Ghigna, P.; Minguzzi, A.; Wierzbicka, E.; Schmuki, P.; Altomare, M. Dewetting of PtCu Nanoalloys on TiO_2 Nanocavities Provides a Synergistic Photocatalytic Enhancement for Efficient H_2 Evolution. *ACS Appl. Mater. Interfaces* **2020**, *12*, 38211–38221.